Journal Pre-proof

Arbitrary High Order Central Non-Oscillatory Schemes on Mixed-Element Unstructured Meshes

Panagiotis Tsoutsanis, Michael Dumbser

PII: S0045-7930(21)00128-6
DOI: https://doi.org/10.1016/j.compfluid.2021.104961
Reference: CAF 104961

To appear in: *Computers and Fluids*

Received date: 6 January 2021
Revised date: 15 March 2021
Accepted date: 8 April 2021

Please cite this article as: Panagiotis Tsoutsanis, Michael Dumbser, Arbitrary High Order Central Non-Oscillatory Schemes on Mixed-Element Unstructured Meshes, *Computers and Fluids* (2021), doi: https://doi.org/10.1016/j.compfluid.2021.104961

This is a PDF file of an article that has undergone enhancements after acceptance, such as the addition of a cover page and metadata, and formatting for readability, but it is not yet the definitive version of record. This version will undergo additional copyediting, typesetting and review before it is published in its final form, but we are providing this version to give early visibility of the article. Please note that, during the production process, errors may be discovered which could affect the content, and all legal disclaimers that apply to the journal pertain.

© 2021 Published by Elsevier Ltd.

Highlights (for review)

Highlights:

- CWENO/CWENOZ methods for mixed-element unstructured meshes
- Analysis of central stencil linear weight selection is given
- Tested for Euler and Navier-Stokes equations
- CWENO/CWENOZ methods more robust and efficient than classical WENO

Computers & Fluids, Volume 225, July 2021, Article number 104961
DOI:10.1016/j.compfluid.2021.104961

Arbitrary High Order Central Non-Oscillatory Schemes on Mixed-Element Unstructured Meshes

Panagiotis Tsoutsanis[a,*], Michael Dumbser[b]

[a]*Centre for Computational Engineering Sciences, Cranfield University, Cranfield MK43 0AL, United Kingdom*
[b]*Department of Civil, Environmental and Mechanical Engineering, University of Trento, Via Mesiano 77,38123 Trento,Italy*

Abstract

In this paper we develop a family of very high-order central (up to 6th-order) non-oscillatory schemes for mixed-element unstructured meshes. The schemes are inherently compact in the sense that the central stencils employed are as compact as possible, and that the directional stencils are reduced in size therefore simplifying their implementation. Their key ingredient is the non-linear combination in a CWENO style similar to Dumbser et al [1] of a high-order polynomial arising from a central stencil with lower-order polynomials from directional stencils. Therefore, in smooth regions of the computational domain the optimum order of accuracy is recovered, while in regions of sharp-gradients the larger influence of the reconstructions from the directional stencils suppress the oscillations. It is the compactness of the directional stencils that increases the chances of at least one of them lying in a region with smooth data, that greatly enhances their robustness compared to classical WENO schemes. The two variants developed are CWENO and CWENOZ schemes, and it is the first time that such very-high-order schemes are designed for mixed-element unstructured meshes. We explore the influence of the linear weights in each of the schemes, and assess their performance in terms of accuracy, robustness and computational cost through a series of stringent 2D and 3D test problems. The results obtained demonstrate the improved robustness that the schemes offer, a parameter of paramount importance for and their potential use for industrial-scale engineering applications.

1. Introduction

The development and application of high-order non-oscillatory schemes for computational fluid dynamics on unstructured meshes has been the focus of an overwhelming number of studies that spans many numerical frameworks and techniques. The catalyst for this development is firstly that arbitrary shaped unstructured elements can offer significant advantages for computational workflows that include complicated geometries that require rapid generated body fitted meshes for flows that are characterised by the presence of phenomena with contradicting requirements. On one hand flows regions with strong gradients or discontinuities require robust non-oscillatory schemes that can resolve the phenomena encountered in these regions without generating spurious oscillations, while on the other hand in regions of smooth flow features, such as vortices or acoustic waves, highly accurate schemes for resolving these delicate flow features is a necessity. Finding the perfect balance between these two contradicting requirements is the driving force upon which the saga towards the ultimate high-order non-oscillatory schemes has been based. To make this situation even more challenging this perfect balance must be obtained in a computationally efficient manner, something that the rapid changing high-performance computing (HPC) landscape makes it harder to sustain since the numerical schemes must be adapted or completely redesigned to make the most of the latest HPC hardware.

The plethora of numerical schemes available in this context are primarily developed in the Finite-Volume (FV) [1–16], discontinuous Galerkin (DG) [17–23], flux reconstruction (FR) [24–31] and spectral-finite-volume (SFV) [32, 33] frameworks. Although the frameworks are significantly different in principle the high-order spatial accuracy

*Corresponding author
Email addresses: panagiotis.tsoutsanis@cranfield.ac.uk (Panagiotis Tsoutsanis), michael.dumbser@unitn.it (Michael Dumbser)

Published by Elsevier. This is the Author Accepted Manuscript issued with: Creative Commons Attribution Non-Commercial No Derivatives License (CC:BY:NC:ND 4.0).
The final published version (version of record) is available online at DOI:10.1016/j.compfluid.2021.104961. Please refer to any applicable publisher terms of use.

is achieved through a natural extension of the representation of the solution within each cell by polynomials. Two of the most popular families of schemes for providing non-oscillatory capabilities to a numerical framework is firstly the family of schemes that can detect when some solution bounds have been violated and switch to a lower-order approximation of the solution such as total-variation bounded (TVB) [34], total-variation diminishing (TVD) [35–37], monotone upstream scheme for conservation laws (MUSCL) [38–46], and multi-dimensional optimal order detection (MOOD) [3, 4, 47–49], and secondly by techniques where the spatial-regions with the best quality of information (smooth data) will have the largest influence in the approximation of the solution, such as the weighted essentially non-oscillatory (WENO) [2, 5, 6, 13, 50–55] schemes. It needs to be noted that high order WENO reconstruction in space is also the key ingredient of the ADER class of finite volume schemes of Toro and Titarev, see e.g. [56–59] and references therein for an overview. The first family is characterised by a compact support stencil (usually a fraction of the central stencil) which is beneficial for the computational efficiency, however these frameworks are not parameter-free and they are rather sensitive to the values of the parameters to define the behaviour of the algorithm once the bounds have been violated as previously reported in [38, 47]. On the other hand, the WENO family of methods offers a high-order accurate platform that is less sensitive to the parameters in particular if transformations are performed to reduce scaling effects [5, 6, 13], and a good computational efficiency, but the size of the directional stencils whose width is dependent on the quality of the mesh is increasing the complexity of the implementation of the schemes as well as their communication overhead across multiple-processes in an HPC setting. One of the ways to alleviate this is to reduce the size of the directional stencils and consequently the order of approximation from them. This strategy has been adopted by many in developing the sometimes called new, central, compact or cool WENO schemes [1, 12, 51, 53, 60–70]. The key benefit of using these schemes is the reduced computational cost compared to the traditional WENO schemes due to the reduced size of the directional stencils. The increased compactness of this class of schemes makes them more suitable to be deployed for frameworks such as DG, something that has already started as seen in [53, 69–71]. However, one of the most overlooked benefits of these type of CWENO schemes is an increased robustness, since the reduced size of the directional stencils translates directly into a higher probability of at least one of them lying in a region with smooth variation of data, compared to the traditional WENO schemes for unstructured meshes. The results obtained with these schemes show a larger sensitivity to the parameters involved, since the blending of a higher-order approximation emanating from the central stencil with lower-order approximation from the directional stencils requires a fine balance and calibration.

In the present study we are pursuing the extension of two variants of central WENO schemes to mixed-element unstructured meshes for an arbitrary high-order. The two variants developed are the CWENO and CWENOZ schemes, where in order to further reduce their computational footprint both variants use the stencil based compact (SBC) central stencil algorithm and Type 3 directional stencil algorithm developed in [72]. For the central stencil the polynomial of any desired order can be built, while for the directional stencils a $\mathcal{P} = 1$ polynomial is employed requiring 4 and 6 neighbours in 2D and 3D respectively. The directional stencils are relatively compact and building them is straight forward since they are contained in the central stencil (at least for higher-order methods) and therefore making the implementation less complicated compared to the original WENO schemes. In this work we develop and apply schemes up to 6th-order of spatial accuracy for mixed-element meshes, and in principle they can be extended to any spatial order. Ultimately the goal is to make this class of very higher-order schemes more affordable and more robust for unstructured meshes even for industrial scale applications.

All the schemes are developed in the open source UCNS3D solver [73], and we assess their performance in terms of robustness, accuracy and computational efficiency for a series of stringent 2D and 3D test problems while also comparing them with the traditional WENO schemes. The paper is organized as follows. In Section 2 we introduce the numerical framework used to describe the high-order finite-volume framework for unstructured meshes, the reconstruction process for the WENO, CWENO and CWENOZ schemes, while describing the chosen fluxes and temporal discretisation employed. The numerical results obtained for all the test problems are presented in Section 3 and compared against analytical, reference or experimental solution whenever possible. Finally, the last section describes the conclusions drawn from this study.

2. Numerical Framework

Consider the unsteady non-linear hyperbolic system of conservation laws on a 3D domain Ω, written in its conservative form:

$$\frac{\partial \mathbf{U}}{\partial t} + \nabla \cdot (\mathbf{F}(\mathbf{U})) = 0, \tag{1}$$

where $\mathbf{U} = \mathbf{U}(\mathbf{x}, t)$ is the vector of conserved variables, $\mathbf{x} = (x, y, z)$ denotes the coordinates of a point of the domain Ω, and $\mathbf{F}(\mathbf{U}) = (\mathbf{f}(\mathbf{U}), \mathbf{g}(\mathbf{U}), \mathbf{h}(\mathbf{U}))$ is the non-linear flux tensor. The physical domain Ω in consists of any combination of conforming tetrahedral, hexahedral, prism or pyramids in 3D, and quadrilateral or triangular 2D. All the elements are indexed by a unique mono-index i. Integrating Eq. (1) over the mesh element i using a high-order explicit finite-volume formulation the following equation is obtained:

$$\mathbf{U}_i^{n+1} = \mathbf{U}_i^n - \Delta t \frac{1}{|V_i|} \sum_{j=1}^{N_f} \sum_{\alpha=1}^{N_{qp}} F^{\mathbf{n}_{ij}} \left(\mathbf{U}_{ij,L}^n(\mathbf{x}_{ij,\alpha}, t), \mathbf{U}_{ij,R}^n(\mathbf{x}_{ij,\alpha}, t) \right) \omega_\alpha |S_{ij}|, \tag{2}$$

where $\mathbf{U}_i$ are the volume averaged conserved variables

$$\mathbf{U}_i = \frac{1}{|V_i|} \int_{V_i} \mathbf{U}(x, y, z)\, dV, \tag{3}$$

and $F^{\mathbf{n}_{ij}}$ is a numerical flux function in the direction normal to the cell interface between cell i and the neighbouring cell j as seen in Fig. 1, N_f is the number of faces per element, N_{qp} is the number of quadrature points used for approximating the surface integrals, $|S_{ij}|$ is the surface area of the corresponding face, and $\mathbf{U}_{ij,L}^n(\mathbf{x}_{ij,\alpha}, t)$ and $\mathbf{U}_{ij,R}^n(\mathbf{x}_{ij,\alpha}, t)$ are the high-order approximations of the solutions for cell i and cell j respectively; while α corresponds to different Gaussian integration points $\mathbf{x}_\alpha$ and weights ω_α over each face. The volume, surface and line integrals are numerically approximated by suitable quadrature rules, see [74] for details on numerical approximations of multiple integrals.

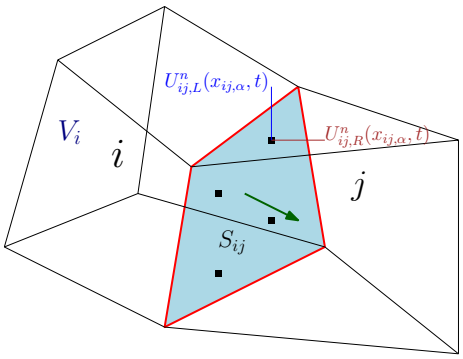

Figure 1: Drawing illustrating the interface between the considered cell i and its neighbour j highlighting the normal vector and the quadrature points at the interface.

2.1. Reconstruction

For a cell i a high-order polynomial $p_i(x, y, z)$ of order r can be built that provides $r + 1$ order of accuracy, by requiring it to have the same average as a general quantity $\mathbf{U}_i$. This can be formulated as:

$$\mathbf{U}_i = \frac{1}{|V_i|} \int_{V_i} p_i(x, y, z)\, dV. \tag{4}$$

The present polynomial reconstruction is based upon the approaches of [5, 6, 13, 52], that have been applied to smooth and discontinuous flow problems [38, 47, 72, 75–86] and only the key-components will be presented herein and the

reader is referred to [5, 6, 52] for further details. Unstructured meshes involve the presence of various elements shapes and sizes, and a transformation from physical space to a reference space is performed to reduce the scaling effects as introduced by Dumbser et al. [13, 14, 87]. In this study this is performed by decomposing each element into triangular or tetrahedral elements and using one of the decomposed elements as the reference element for transforming to the new system of coordinates as suggested by Tsoutsanis et al. [5, 6, 52]. The decomposition strategy is discussed in [6].

Let $\mathbf{vx}_{ij}$, $j = 1, 2, \dots J_i$ be the vertices of the considered 3D general element. Non tetrahedral elements are decomposed into tetrahedrals and one of them is chosen with $\mathbf{w}_1 = (x_1, y_1, z_1)$, $\mathbf{w}_2 = (x_2, y_2, z_2)$, $\mathbf{w}_3 = (x_3, y_3, z_3)$ and $\mathbf{w}_4 = (x_4, y_4, z_4)$ being its four vertices. The transformation from the Cartesian coordinates x, y, z into a reference space ξ, η, ζ is given by the following equations:

$$\begin{pmatrix} x \\ y \\ z \end{pmatrix} = \begin{pmatrix} x_1 \\ y_1 \\ z_1 \end{pmatrix} + J \cdot \begin{pmatrix} \xi \\ \eta \\ \zeta \end{pmatrix}, \tag{5}$$

with the Jacobian matrix given by:

$$J = \begin{bmatrix} x_2 - x_1 & x_3 - x_1 & x_4 - x_1 \\ y_2 - y_1 & y_3 - y_1 & y_4 - y_1 \\ z_2 - z_1 & z_3 - z_1 & z_4 - z_1 \end{bmatrix}. \tag{6}$$

Using an inverse mapping the element V_i can be transformed to the element V_i' in the reference co-ordinate system as:

$$\mathbf{vx}'_{ij} = J^{-1} \cdot \left(\mathbf{vx}_{ij} - \mathbf{w}_1 \right), \quad j = 1, 2, \dots J_i. \tag{7}$$

and the spatial average of the conserved variable $\mathbf{U}_i$ does not change during transformation

$$\mathbf{U}_i = \frac{1}{|V_i|} \int_{V_i} \mathbf{U}(x, y, z)\, dV \equiv \frac{1}{|V_i'|} \int_{V_i'} \mathbf{U}(\xi, \eta, \zeta)\, d\xi d\eta d\zeta. \tag{8}$$

The reconstruction is performed by building a central stencil $\mathcal{S}^1$ by recursively adding neighbouring elements, consisting of $M + 1$ cells including the considered cell i. In this study the stencil based compact algorithm (SBC) introduced in [72] is used due to its low computational cost and enhanced robustness, the reader is referred to [72] for more details. In the present study we employ $M = 2K$, for enhanced robustness as reported in several previous studies [3–5, 13, 72, 87–89], where K is the total number of polynomial coefficients given by:

$$K(r, d) = \frac{1}{d!} \prod_{l=1}^{d} (r + l), \tag{9}$$

where $d \in [2, 3]$ is the number of space dimensions. The central stencil $\mathcal{S}^1$ is given by

$$\mathcal{S}_i^c = \bigcup_{m=0}^{M_c} V_m, \tag{10}$$

where the index m refers to the local numbering of the elements in the stencil with the element with index 0 being the considered cell i, and the index c referring to the stencil number (in case of multiple stencils) where for the central stencil $c = 1$. The entire stencil of the considered cell i is transformed in reference space $\mathcal{S}'^c_i$, where the r^{th} order reconstruction polynomial is an expansion over local polynomial basis functions $\phi_k(\xi, \eta, \zeta)$ given by:

$$p(\xi, \eta, \zeta) = \sum_{k=0}^{K} a_k \phi_k(\xi, \eta, \zeta) = \mathbf{U}_0 + \sum_{k=1}^{K} a_k \phi_k(\xi, \eta, \zeta), \tag{11}$$

where $\mathbf{U}_0$ corresponds to the vector of conserved variables at the considered cell i, and a_k are the degrees of freedom of the polynomial. The degrees of freedom a_k for the polynomial for each cell m are obtained by satisfying the condition

that the cell average of the reconstruction polynomial $p(\xi,\eta,\zeta)$ must be equal to the cell average of the solution $\mathbf{U}_m$:

$$\int_{V'_m} p(\xi,\eta,\zeta)\, d\xi d\eta d\zeta = |V'_m|\mathbf{U}_0 + \sum_{k=1}^{K} \int_{V'_m} a_k \phi_k \, d\xi d\eta d\zeta = |V'_m|\mathbf{U}_m, \quad m = 1,\ldots,M. \tag{12}$$

It needs to be stressed that since for hexahedral, quadrilateral, prisms and pyramid cells the transformation to reference space into a unit element cell cannot be guaranteed, the basis functions ψ_k also need to satisfy equation (4). The basis functions employed ψ_k for all the elements in the stencil are defined as follows:

$$\phi_k(\xi,\eta,\zeta) \equiv \psi_k(\xi,\eta,\zeta) - \frac{1}{|V'_0|}\int_{V'_0} \psi_k \, d\xi d\eta d\zeta \quad k = 1,2,\ldots,K, \tag{13}$$

and in the present study ψ_k are Legendre polynomials basis functions. Denoting the integrals of the basis function k over the cell m in the stencil, and the vector of right-hand side by A_{mk} and b respectively as given by

$$A_{mk} = \int_{V'_m} \phi_k \, d\xi d\eta d\zeta, \quad b_m = |V'_m|(\mathbf{U}_m - \mathbf{U}_0),$$

the equations for degrees of freedom a_k can be rewritten in a matrix form as:

$$\sum_{k=1}^{K} A_{mk} a_k = b_m, \quad m = 1,2,\ldots M. \tag{14}$$

The resulting linear system is solved by a QR decomposition based on Householder transformation [90] while using a Moore-Penrose pseudo-inverse of A_{mk} which is only computed once at the beginning of the simulation as detailed in [72].

2.1.1. WENO Scheme

The WENO scheme used in this study, employs a non-linear combination of various reconstruction polynomials from the central stencil and additional directional stencils; each polynomial is weighted according to the smoothness of its solution, and it is based on the approaches of [5, 6, 13, 87]. The polynomials are given as:

$$p_i(\xi,\eta,\zeta)^{\text{weno}} = \sum_{s=1}^{s_t} \omega_s p_s(\xi,\eta,\zeta), \tag{15}$$

where s_t is the total number of stencils. Substituting back to Eq. (11) for $p_s(\xi,\eta,\zeta)$, we obtain the following expression:

$$p_s\,(\xi,\eta,\zeta) = \sum_{k=0}^{K} a_k^{(s)} \phi_k(\xi,\eta,\zeta). \tag{16}$$

Using the condition that the sum of all weights is unity, yields:

$$\begin{aligned} p_i(\xi,\eta,\zeta)^{\text{weno}} &= \mathbf{U}_0 + \sum_{k=1}^{K}\left(\sum_{s=0}^{s_t} \omega_s a_k^s\right)\phi_k(\xi,\eta,\zeta) \\ &\equiv \mathbf{U}_0 + \sum_{k=1}^{K} \tilde{a}_k \phi_k(\xi,\eta,\zeta), \end{aligned} \tag{17}$$

where $\tilde{a}_k$ are the reconstructed degrees of freedom; and the non-linear weight ω_m is defined as:

$$\omega_s = \frac{\tilde{\omega}_s}{\sum_{s=1}^{s_t} \tilde{\omega}_s} \quad \text{where} \quad \tilde{\omega}_s = \frac{\lambda_s}{(\epsilon + \mathcal{SI}_s)^b}. \tag{18}$$

The smoothness indicator $\mathcal{SI}_m$ is given by:

$$\mathcal{SI}_s = \sum_{1 \le |\beta| \le r} \int_{V_0'} \left(\mathcal{D}^\beta p_s(\xi, \eta, \zeta)\right)^2 (d\xi, d\eta, d\zeta), \tag{19}$$

where β is a multi-index, r is the polynomial's order, λ_m is the linear weight. The central stencil is assigned a large linear weight λ_1 (to be discussed later), while the remaining directional stencils are assigned a value of $\lambda_s = 1$ and a value to prevent division by zero of $\epsilon = 10^{-6}$ is used, $b = 4$ and $\mathcal{D}$ is the derivative operator. It must be stressed that the purpose of the linear weights in this WENO type of method is not to recover an optimal polynomial, but rather to give a larger influence to the more symmetric central stencil in regions of smooth gradients as detailed in [5, 6, 13, 87].

The smoothness indicator is a quadratic function of the degrees of freedom (a_k^s) and Eq. (19) can be rewritten as:

$$\mathcal{SI}_s = \sum_{k=1}^{K} a_k^s \left(\sum_{q=1}^{K} \mathcal{OI}_{kq} a_q^s \right), \tag{20}$$

where the oscillation indication matrix $\mathcal{OI}_{kq}$ is given by:

$$\mathcal{OI}_{kq} = \sum_{1 \le |\beta| \le r} \int_{V_0'} \left(\mathcal{D}^\beta \phi_k(\xi, \eta, \zeta)\right)\left(\mathcal{D}^\beta \phi_q(\xi, \eta, \zeta)\right) (d\xi, d\eta, d\zeta), \tag{21}$$

and can be precomputed and stored at the beginning of the simulation. Additionally the WENO reconstruction can be carried out with respect to the characteristic variables, and the reader is referred to [5, 6, 52] and references therein regarding the implementation. Although the use of characteristic decomposition in reconstruction increases the computational cost of the schemes significantly, previous experiments [91] have demonstrated that that in some cases it is necessary in order to avoid spurious oscillations for WENO type of schemes, in particular for cases with strong shocks and contact discontinuities as reported by Harten et al. [92]. For the directional stencils the Type3 algorithm introduced in [72] is employed and in Fig. 2 a typical representation of them can be seen.

2.1.2. CWENO Scheme

One of the key ingredients of the CWENO scheme is the combination of an optimal (high-order) polynomial p_{opt} using the central stencil with lower-order polynomials employing the directional stencils. At the presence of smooth data the optimal polynomial is recovered and therefore the desired-order of accuracy is obtained, whereas at the presence of discontinuous data at least one of the lower-order polynomials arising from the directional stencils could contain smooth data, hence essentially reducing the oscillations in the computed solution. All the polynomials involved are subject to the same requirements as previously set of matching the cell averages of the solution, and all of them are overdetermined linear systems solved with the same constrained least-squares technique. The directional stencils employ the Type3 definition as set in [72]. The computational savings compared to the WENO schemes arise from the reduced size of the directional stencils, and the fact that the directional stencils are contained in the central stencil as it can be seen in Fig. 2. The definition of an optimal polynomial given by:

$$p_{opt}(\xi, \eta, \zeta) = \sum_{s=1}^{s_t} \lambda_s p_s(\xi, \eta, \zeta), \tag{22}$$

where s is the stencil index, with $c = 1$ being the central, $c = 2, 3, .$ being the directional, s_t being the total number of stencils, and λ_s being the linear coefficients for each stencil, whose sum is equal to 1. The p_1 polynomial is

not computed directly, but computed by subtracting the lower-order polynomials from the optimum polynomial as follows:

$$p_1(\xi,\eta,\zeta) = \frac{1}{\lambda_1}\left(p_{opt}(\xi,\eta,\zeta) - \sum_{s=2}^{s_t} \lambda_s p_s(\xi,\eta,\zeta)\right). \tag{23}$$

It needs to be noted that the cost of computing p_1 polynomial is significantly higher than a similar order polynomial, since we need to performe the substractions of the contributions of the lower-order polynomials. This will be seen later on to have a significant impact on the performance of the schemes. The CWENO reconstruction polynomial is given as a non-linear combination of all the polynomials in the following manner:

$$p(\xi,\eta,\zeta)^{\text{cweno}} = \sum_{s=1}^{s_t} \omega_s p_s(\xi,\eta,\zeta), \tag{24}$$

where ω_s correspond to the non-linear weights assigned to each polynomial, and in regions with smooth data $\omega_s \approx \lambda_s$, hence obtaining the high-order approximation from the central stencil, and in regions of discontinuous solutions the reconstructed solution will be mostly influenced from the lower-order polynomials of the directional stencils. where $\tilde{a}_k$ are the reconstructed degrees of freedom; and the non-linear weight ω_s is defined as:

$$\omega_s = \frac{\tilde{\omega}_s}{\sum_{s=1}^{s_t} \tilde{\omega}_s} \quad \text{where} \quad \tilde{\omega}_s = \frac{\lambda_s}{(\epsilon + \mathcal{SI}_s)^b}. \tag{25}$$

Similarly, to the WENO scheme $\epsilon = 10^{-6}$ is used and $b = 4$. For the present study we employ $r = 1$ for the directional polynomials resulting in 2nd-order of accuracy, and any arbitrary order of accuracy for the polynomial associated with the central stencil. The smoothness indicators used for CWENO scheme are the same as in the WENO scheme defined previously. It needs to be stressed however that since polynomials of different orders are involved the smoothness indicators are also corresponding to polynomials of different order, and all of them have the same influence on the approximation of the non linear weights. The linear weights are assigned by firstly assigning the non-normalised linear weight for the central stencil $\lambda_1^{'}$ an arbitrary value, and then normalising this as follows:

$$\lambda_1 = 1 - \frac{1}{\lambda_1^{'}}, \tag{26}$$

with the linear weights associated with lower-order polynomials being assigned the same linear weights as follows:

$$\lambda_s = \frac{1-\lambda_1}{s_t - 1}, \tag{27}$$

where s_t is the total number of stencils.

2.1.3. CWENOZ Scheme

The CWENOZ scheme follows in principle the CWENO scheme, the main difference being the approximation of the non-linear weights. As previously a high-order polynomial is combined with lower-order polynomials arising from the directional stencils also using the Type3 definition as set in [72]. The definition of the optimal polynomial remains the same as before and the CWENOZ reconstruction polynomial is given as a non-linear combination of all the polynomials in the following manner:

$$p(\xi,\eta,\zeta)^{\text{cwenoz}} = \sum_{s=1}^{s_t} \omega_s p_s(\xi,\eta,\zeta), \tag{28}$$

where ω_s correspond to the non-linear weights assigned to each polynomial. The characteristic difference is the approximation of the non-linear weights ω_s. We mentioned previously that the smoothness indicators for the CWENO scheme arise from polynomials of different orders. The WENOZ component of combining unequal degree polyno-

mials as introduced by Borges et al. and Castro et al. [93, 94] is employed in this study, but adapted for unequal polynomials, sized reconstruction stencils and arbitrary elements as has recently been reported by [67, 68] . The non-linear weights are now defined as:

$$\omega_s = \frac{\tilde{\omega}_s}{\sum_{s=1}^{s_t} \tilde{\omega}_s} \quad \text{where} \quad \tilde{\omega}_s = \lambda_s \left(1 + \frac{\tau}{\epsilon + \mathcal{SI}_s}\right). \tag{29}$$

With τ being the universal oscillation indicator and taken as the absolute difference between the smoothness indicators as follows:

$$\tau = \left(\frac{\sum_{s=2}^{s_t} |\mathcal{SI}_s - \mathcal{SI}_1|}{s_t - 1} \right)^b. \tag{30}$$

Similarly to the WENO scheme $\epsilon = 10^{-6}$ is used and $b = 4$. For the present study we employ $r = 1$ for the directional polynomials resulting in 2nd-order of accuracy, and any arbitrary order of accuracy for the polynomial associated with the central stencil. The procedure for the assignment of the linear weights is similar to the CWENO approach described previously. A more sophisticated way to computing the coefficient b, could follow the paradigm of Semplice and Visconti [61] and Cravero et al. [95] where a series of comprehensive studies for various parameters, including b and ϵ has been performed for obtaining the optimal convergence rates of the designed schemes for structured meshes. Therefore the expansion of this optimisation to unstructured meshes could further fortify the CWENOZ schemes.

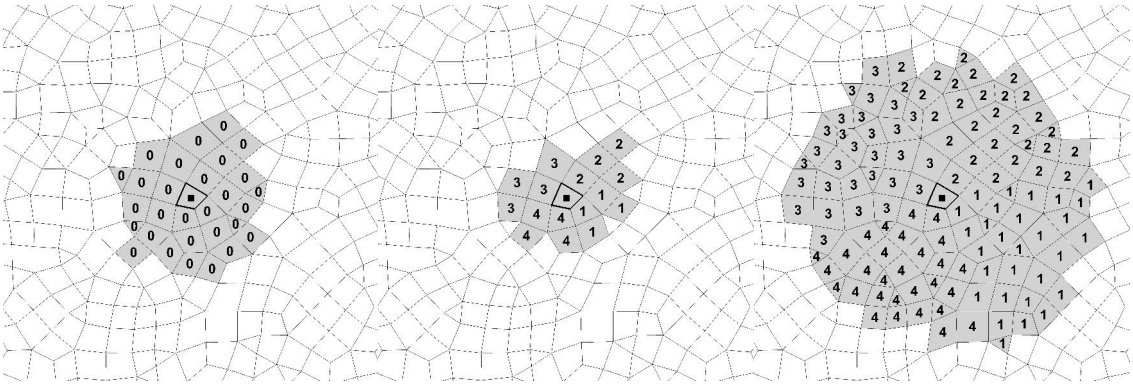

(a) Central Stencil (b) CWENO/CWENOZ directional stencils (c) WENO directional stencils

Figure 2: Examples of central and directional stencils for $\mathcal{P} = 4$ for the WENO, and CWENO/CWENOZ schemes. The considered cell is illustrated by bold lines, the elements of the central stencil indicated by the number 0 and the elements of each of the directional stencils indicated by the numbers 1, 2, 3 and 4. It can be noticed that the CWENO/Z schemes employ significantly smaller directional stencils compared to WENO schemes.

2.2. *Fluxes approximation & Temporal discretisation*

For the inviscid fluxes the approximate HLLC (Harten-Lax-van Leer-Contact) Riemann solver of Toro [96] is employed, unless otherwise stated. For the viscous stress tensor and the heat flux vector in the Navier-Stokes equations the gradients of the discontinuous states for the approximation of the viscous fluxes are averaged by including the penalty terms similar to previous approaches [97–99] in the following manner:

$$\nabla \mathbf{U} = \frac{1}{2} \left(\nabla \mathbf{U}_L + \nabla \mathbf{U}_R\right) + \frac{\alpha}{L_{int}} \left(\mathbf{U}_R - \mathbf{U}_L\right) \vec{n}, \tag{31}$$

where L_{int} is the distance between the cell centres of adjacent cells, and $\alpha = 4/3$ similarly to previous approaches [97, 98]. The gradients are obtained through the unlimited k-exact least square reconstruction utilising the central stencil as previously described in [6, 11], although a weighted least-squares reconstruction could also be employed it was dismissed since from a comprehensive previous study [72] it was documented that it offered a marginal improvement for the solution approximation but no improvement for the gradients approximation. The temporal discretisation employs the 4^{th}-order explicit Strong Stability Preserving (SSP) Runge-Kutta method of Spiteri and Ruuth [100] which is stable for $CFL \approx 1.50$. The minimum timestep size is defined as follows:

$$\Delta t = min\left(\frac{1}{d \cdot (\frac{s_i}{h_i} + \frac{(\mu+\kappa)}{2 \cdot h_i^2})}\right), \tag{32}$$

where d refers to the number of dimensions, s_i is the maximum eigenvalue for the convective flux jacobian as $s_i = max(|u_i|, |v_i|, |w_i|) + a_i$, with u, v, w being the cartesian velocity components, and a_i being the speed of sound, Finally, the μ and κ correspond to the dynamic viscosity and thermal conductivity coefficient.

All the volume/surface/line integrals are approximated by Gaussian quadrature rule suitable for the order of polynomial employed, while for the initialisation the control volume averages are obtained with a 7th-order Gaussian quadrature to ensure consistent initial conditions across all the schemes. All the schemes developed are implemented in the UCNS3D CFD code [73] which is written in object-oriented Fortran 2003, employing MPI message passing interface (MPI), and the Open Multi-Processing (OpenMP) application programming interface (API), and the reader is referred to [86, 101] for more details on implementation and performance benchmarks. The computational times reported in each case are obtained for the same hardware (and compilation settings) and normalised with respect to a reference setup for the same hardware so that the performance of various algorithms under the same hardware can be appreciated.

3. Applications

We present the numerical simulations employed to assess the performance of the CWENO and CWENOZ schemes in terms of robustness, accuracy and computational efficiency for the solution of the Euler and Navier-Stokes equations. Several benchmark test problems have been performed and are listed below:

- 2D Vortex Evolution. This test problem provides an assessment of the accuracy and computational footprint of the methods. The influence of the central stencil linear weight is also investigated.
- 2D Solid Body Rotation. This test problem is ideal for assessing simultaneously the accuracy and non-oscillatory behaviour of the schemes.
- Shu-Osher Problem. This test problem provides an assessment of the non-oscillatory properties of the methods in combination with smooth flow features.
- 2D Riemann Problem. Apart from the non-oscillatory properties of the schemes the impact of the characteristics-based reconstruction is explored for this test case.
- Taylor Green Vortex. A well-established test problem for assessing the ILES capabilities of the schemes. This test is used for establishing the computational cost of all the schemes in a 3D setting.
- Schardin's problem. This test problem is used to assess the performance of a scheme in a flow problem characterised by the presence of strong-gradients regions interacting with vortices and compare with the experimental results.
- Transonic Cylinder $Re = 3900$. A test problem involving the interactions of the vortices at the cylinder wake with shocks and therefore being ideal for demonstrating the capability of a numerical scheme to resolve these.

3.1. 2D Vortex Evolution

The 2D vortex evolution test problem proposed by Balsara and Shu [102] is used, involving an isentropic vortex propagating at supersonic Mach number at 45° across the domain modelled by the unsteady inviscid Euler equations. The computational domain is given by $[0, 10] \times [0, 10]$ with periodic boundary conditions applied on all sides. The unperturbed domain has an initial condition $(\rho, u, v, p) = (1, 1, 1, 1)$, where temperature and density are defined as $T = p/\rho$, and $S = p/\rho^{\gamma}$ the adiabatic gas constant $\gamma = 1.4$ and the vortex perturbations are given by:

$$\delta T = -\frac{(\gamma - 1)\,\epsilon^2}{8\gamma\pi^2} e^{(1-r^2)}, \qquad (\delta u, \delta v) = \frac{\epsilon}{2\pi} e^{0.5(1-r^2)} \left(-(y-5), (x-5)\right). \tag{33}$$

The vortex strength $\epsilon = 5$ and adiabatic gas constant $\gamma = 1.4$. The e_{L^2} and the e_{L^∞} errors are computed as follows:

$$e_{L^2} = \sqrt{\frac{\sum_i \int_{\Omega_i} \left(\mathbf{U}_e\left(x, t_f\right) - \mathbf{U}_c\left(x, t_f\right)\right)^2 dV}{\sum_i |\Omega_i|}}, \tag{34}$$

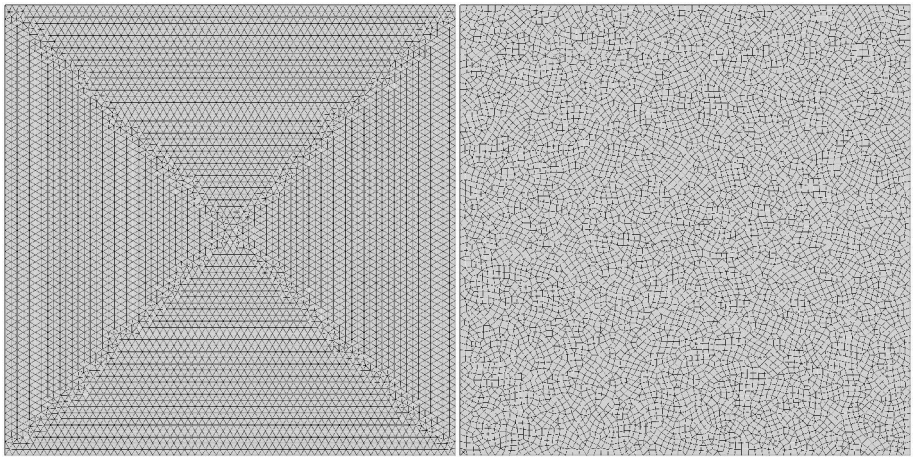

(a) *Triangular* (b) *Hybrid*

Figure 3: Meshes used for the 2D vortex evolution test problem.

$$e_{L^\infty} = \mathcal{M}ax \left| \left(\mathbf{U}_e\left(x, t_f\right) - \mathbf{U}_c\left(x, t_f\right)\right) \right|, \tag{35}$$

where $\mathbf{U}_c\left(x, t_f\right)$ and $\mathbf{U}_e\left(x, t_f\right)$ are the computed and exact solutions at the end of the simulation t_f. The exact solution $\mathbf{U}_e\left(x, t_f\right)$ being given by the initial condition itself at t_0. Two types of unstructured meshes a triangular and a hybrid one as shown in Fig. 3 are used for this test problem of 16,32,64 and 128 edges per side resolution, and the simulation is run for a time of $t_f = 10$. The purpose of this test problem is to assess the performance of the CWENO and CWENOZ schemes in terms of accuracy, sensitivity to central stencil linear weight, and computational cost against the traditional WENO scheme and unlimited linear schemes. Therefore, schemes ranging from 3rd- to 6th-order of spatial accuracy are employed, and all the WENO variants are assessed using three different values for their central stencil linear weight. To assess the computational cost of the schemes, the time taken for completing each run for the non-linear schemes has been normalised with respect to the time taken by the unlimited linear scheme of equal order of accuracy, at the exact same grid type and resolution and CPU hardware. In this manner a more representative computational footprint of the non-linear schemes is provided. Ideally we would like to determine the smallest value of central stencil linear weight required to achieve the designed order of accuracy, given that WENO, CWENO and CWENOZ will achieve under different conditions. This will be later one used to assess the non-oscillatory properties

of the schemes, so that the central stencil linear weight selected should be suitable to allow the scheme to reach the designed order of spatial accuracy in smooth regions of the flow.

From the obtained results of the unlimited linear schemes as listed in Table 1, it is clear that all the schemes achieve convergence rates close to their theoretical ones. Although for the 5th and 6th-order schemes a timestep size significantly smaller than the one employed with the current time discretisation would have been required to achieve exactly the theoretical ones, but this is beyond the scope of the present study.

Table 1: e_{L^∞} and e_{L^2} error, and convergence rates O_{L^∞} , O_{L^∞} of density for the 2D vortex evolution test problem at the final time of $t = 10$, obtained with the linear (unlimited) scheme using various spatial order of accuracy approximations ranging from 3rd-($\mathcal{P}2$ Reconstruction Polynomial) to 6th-order ($\mathcal{P}5$ Reconstruction Polynomial). It can be noticed that all the variants achieve convergence rates close to their theoretical ones.

	Triangular Mesh				Hybrid Mesh			
Order/Number of Edges	e_{L^∞}	O_{L^∞}	e_{L^2}	O_{L^2}	e_{L^∞}	O_{L^∞}	e_{L^2}	O_{L^2}
$\mathcal{P}2/16$	1.830E-01	0.00	2.266E-02	-	2.828E-01	-	3.620E-02	-
$\mathcal{P}2/32$	3.478E-02	2.40	5.057E-03	2.16	7.661E-02	1.88	1.008E-02	1.84
$\mathcal{P}2/64$	6.089E-03	2.51	9.271E-04	2.45	1.268E-02	2.60	1.878E-03	2.42
$\mathcal{P}2/128$	7.862E-04	2.95	1.257E-04	2.88	1.891E-03	2.74	2.767E-04	2.76
$\mathcal{P}3/16$	3.559E-02	-	5.361E-03	-	1.035E-01	-	1.364E-02	-
$\mathcal{P}3/32$	9.397E-03	1.92	8.548E-04	2.65	2.932E-02	1.82	2.450E-03	2.48
$\mathcal{P}3/64$	3.942E-04	4.58	4.827E-05	4.15	9.213E-04	4.99	1.489E-04	4.04
$\mathcal{P}3/128$	2.737E-05	3.85	3.043E-06	3.99	6.475E-05	3.83	7.436E-06	4.32
$\mathcal{P}4/16$	5.131E-02	-	6.727E-03	-	1.348E-01	-	1.632E-02	-
$\mathcal{P}4/32$	1.557E-02	1.72	1.290E-03	2.38	2.992E-02	2.17	2.702E-03	2.59
$\mathcal{P}4/64$	4.223E-04	5.20	6.881E-05	4.23	1.011E-03	4.89	1.599E-04	4.08
$\mathcal{P}4/128$	1.510E-05	4.81	2.520E-06	4.77	4.188E-05	4.59	6.426E-06	4.64
$\mathcal{P}5/16$	5.532E-02	-	4.804E-03	-	4.396E-02	-	6.456E-03	-
$\mathcal{P}5/32$	2.229E-03	4.63	2.930E-04	4.04	1.357E-02	1.70	1.019E-03	2.66
$\mathcal{P}5/64$	7.700E-05	4.86	8.411E-06	5.12	2.307E-04	5.88	2.566E-05	5.31
$\mathcal{P}5/128$	1.672E-06	5.53	4.616E-07	4.19	3.946E-06	5.87	6.382E-07	5.33

From the WENO schemes results listed in Table 2, all the variants reach convergence rates close to their theoretical ones and similar errors to the unlimited linear schemes. The obtained convergence rates are not particularly sensitive to the choice of the central stencil linear weight as also previously documented in [13, 14]. The computational cost of the WENO schemes is approximately 3.4 times higher than the equivalent unlimited scheme. From this study a linear weight of $\lambda_1 = 10^3$ will be used hereafter for WENO scheme.

From the CWENO schemes results listed in Table 3, it can be noticed that the convergence rates are particularly sensitive to the choice of the central stencil linear weight. Firstly the linear weight $\lambda_1 = 10^3$ is clearly unsuitable for all discretisation orders and mesh resolutions. The linear weight $\lambda_1 = 10^7$ is providing a better performance compared to the smaller one, but as the spatial order of accuracy of the scheme increases the performance deteriorated. On the other hand, with an excessively large central stencil linear weight of $\lambda_1 = 10^{15}$ the obtained performance is close to the equivalent unlimited linear scheme. The unscaled smoothness indicators arising from polynomials of different orders of accuracy prevent the CWENO schemes from realising their full potential (especially for higher-order polynomials), unless an excessive large central stencil linear weight is used. On the positive side the computational cost of the CWENO schemes is approximately 2.4 times higher than the equivalent unlimited scheme, therefore establishing them as preferred alternative to WENO schemes in terms of cost. From this study a linear weight of $\lambda_1 = 10^{15}$ will be the selected one for the CWENO scheme.

The CWENOZ schemes achieve convergence rates close to the theoretical ones as shown in Table 4, while not being sensitive to the choice of the central stencil linear weight. It needs to be highlighted that this desirable insensi-

Table 2: e_{L^∞} and e_{L^2} error, convergence rates O_{L^∞} , O_{L^∞} of density, and normalised CPU cost (normalised with respect to the CPU time taken for the equivalent unlimited scheme at the same grid resolution) for the 2D vortex evolution test problem at the final time of $t = 10$ obtained with the WENO schemes using various spatial order of accuracy approximations ranging from 3rd-($\mathcal{P}2$ Reconstruction Polynomial) to 6th-order ($\mathcal{P}5$ Reconstruction Polynomial), and linear weight λ_1 for the central stencil. It can be noticed that all the variants achieve convergence rates close to their theoretical ones, the dependence of the convergence rates to the central stencil linear weight is limited, while being approximately 3.4 times more expensive than the equivalent unlimited scheme.

Order/Number of Edges	$\lambda_1 = 10^3$				$\lambda_1 = 10^6$				$\lambda_1 = 10^9$				Cost
Triangular Mesh	e_{L^∞}	O_{L^∞}	e_{L^2}	O_{L^2}	e_{L^∞}	O_{L^∞}	e_{L^2}	O_{L^2}	e_{L^∞}	O_{L^∞}	e_{L^2}	O_{L^2}	CPU
$\mathcal{P}2/16$	1.934E-01	-	2.449E-02	-	1.833E-01	-	2.272E-02	-	1.830E-01	-	2.266E-02	-	3.326
$\mathcal{P}2/32$	3.430E-02	2.50	4.881E-03	2.33	3.478E-02	2.40	5.056E-03	2.17	3.478E-02	2.40	5.057E-03	2.16	2.947
$\mathcal{P}2/64$	6.059E-03	2.50	9.202E-04	2.41	6.089E-03	2.51	9.271E-04	2.45	6.089E-03	2.51	9.271E-04	2.45	3.773
$\mathcal{P}2/128$	7.818E-04	2.95	1.249E-04	2.88	7.862E-04	2.95	1.257E-04	2.88	7.862E-04	2.95	1.257E-04	2.88	3.412
$\mathcal{P}3/16$	4.107E-02	-	6.814E-03	-	3.633E-02	-	5.422E-03	-	3.568E-02	-	5.364E-03	-	3.033
$\mathcal{P}3/32$	9.258E-03	2.15	8.254E-04	3.05	9.398E-03	1.95	8.547E-04	2.67	9.397E-03	1.92	8.548E-04	2.65	3.195
$\mathcal{P}3/64$	3.900E-04	4.57	4.761E-05	4.12	3.942E-04	4.58	4.827E-05	4.15	3.942E-04	4.58	4.827E-05	4.15	3.051
$\mathcal{P}3/128$	2.708E-05	3.85	3.013E-06	3.98	2.737E-05	3.85	3.043E-06	3.99	2.737E-05	3.85	3.043E-06	3.99	2.999
$\mathcal{P}4/16$	6.070E-02	-	8.459E-03	-	5.129E-02	-	6.720E-03	-	5.132E-02	-	6.727E-03	-	3.224
$\mathcal{P}4/32$	1.550E-02	1.97	1.285E-03	2.72	1.557E-02	1.72	1.290E-03	2.38	1.557E-02	1.72	1.290E-03	2.38	3.158
$\mathcal{P}4/64$	4.222E-04	5.20	6.876E-05	4.22	4.223E-04	5.20	6.881E-05	4.23	4.223E-04	5.20	6.881E-05	4.23	3.483
$\mathcal{P}4/128$	1.513E-05	4.80	2.524E-06	4.77	1.510E-05	4.81	2.520E-06	4.77	1.510E-05	4.81	2.520E-06	4.77	3.183
$\mathcal{P}5/16$	3.887E-02	-	4.751E-03	-	5.537E-02	-	4.846E-03	-	5.533E-02	-	4.803E-03	-	3.299
$\mathcal{P}5/32$	2.238E-03	4.12	2.959E-04	4.01	2.229E-03	4.63	2.930E-04	4.05	2.229E-03	4.63	2.930E-04	4.04	3.249
$\mathcal{P}5/64$	7.729E-05	4.86	8.494E-06	5.12	7.700E-05	4.86	8.411E-06	5.12	7.700E-05	4.86	8.411E-06	5.12	3.541
$\mathcal{P}5/128$	1.686E-06	5.52	4.620E-07	4.20	1.672E-06	5.53	4.616E-07	4.19	1.672E-06	5.53	4.616E-07	4.19	3.663
Hybrid Mesh	e_{L^∞}	O_{L^∞}	e_{L^2}	O_{L^2}	e_{L^∞}	O_{L^∞}	e_{L^2}	O_{L^2}	e_{L^∞}	O_{L^∞}	e_{L^2}	O_{L^2}	CPU
$\mathcal{P}2/16$	3.177E-01	-	4.259E-02	-	2.914E-01	-	3.767E-02	-	2.839E-01	-	3.641E-02	-	3.364
$\mathcal{P}2/32$	8.134E-02	1.97	9.919E-03	2.10	7.661E-02	1.93	1.005E-02	1.91	7.661E-02	1.89	1.008E-02	1.85	3.518
$\mathcal{P}2/64$	1.244E-02	2.71	1.809E-03	2.46	1.267E-02	2.60	1.878E-03	2.42	1.268E-02	2.60	1.878E-03	2.42	3.482
$\mathcal{P}2/128$	1.871E-03	2.73	2.730E-04	2.73	1.891E-03	2.74	2.767E-04	2.76	1.891E-03	2.74	2.767E-04	2.76	3.005
$\mathcal{P}3/16$	1.638E-01	-	2.468E-02	-	1.151E-01	-	1.604E-02	-	1.044E-01	-	1.386E-02	-	3.187
$\mathcal{P}3/32$	2.743E-02	2.58	2.226E-03	3.47	2.923E-02	1.98	2.429E-03	2.72	2.931E-02	1.83	2.449E-03	2.50	3.647
$\mathcal{P}3/64$	8.979E-04	4.93	1.441E-04	3.95	9.212E-04	4.99	1.489E-04	4.03	9.213E-04	4.99	1.489E-04	4.04	3.352
$\mathcal{P}3/128$	6.263E-05	3.84	7.166E-06	4.33	6.474E-05	3.83	7.436E-06	4.32	6.475E-05	3.83	7.436E-06	4.32	3.314
$\mathcal{P}4/16$	1.747E-01	-	2.308E-02	-	1.415E-01	-	1.763E-02	-	1.358E-01	-	1.647E-02	-	4.422
$\mathcal{P}4/32$	2.939E-02	2.57	2.617E-03	3.14	2.990E-02	2.24	2.697E-03	2.71	2.992E-02	2.18	2.702E-03	2.61	3.938
$\mathcal{P}4/64$	1.015E-03	4.86	1.599E-04	4.03	1.011E-03	4.89	1.599E-04	4.08	1.011E-03	4.89	1.599E-04	4.08	3.880
$\mathcal{P}4/128$	4.239E-05	4.58	6.497E-06	4.62	4.188E-05	4.59	6.426E-06	4.64	4.188E-05	4.59	6.426E-06	4.64	3.618
$\mathcal{P}5/16$	1.003E-01	-	1.397E-02	-	5.540E-02	-	7.847E-03	-	4.449E-02	-	6.580E-03	-	3.598
$\mathcal{P}5/32$	1.270E-02	2.98	9.734E-04	3.84	1.357E-02	2.03	1.016E-03	2.95	1.357E-02	1.71	1.018E-03	2.69	3.878
$\mathcal{P}5/64$	2.161E-04	5.88	2.635E-05	5.21	2.307E-04	5.88	2.566E-05	5.31	2.307E-04	5.88	2.566E-05	5.31	4.180
$\mathcal{P}5/128$	4.177E-06	5.69	6.582E-07	5.32	3.946E-06	5.87	6.382E-07	5.33	3.946E-06	5.87	6.382E-07	5.33	4.199

tivity to the choice of the central stencil linear weight is the result of the scaling of the smoothness indicators arising from polynomials of different orders of accuracy. The computational cost of the CWENOZ schemes is similar to the CWENO schemes and approximately 2.4 times higher than the equivalent unlimited scheme. From this study a central stencil linear weight of $\lambda_1 = 0.9$ will be the selected one for CWENOZ.

3.2. 2D Solid Body Rotation

The solid body rotation test of Leveque [103] is employed to investigate the performance of the WENO, CWENO and CWENOZ schemes in terms of their non-oscillatory properties on the correct and accurate revolution of a body. The continuity equation is considered as follows:

$$\frac{\partial U}{\partial t} + \nabla \cdot (\mathbf{v}U) = 0, \tag{36}$$

Table 3: e_{L^∞} and e_{L^2} error, convergence rates O_{L^∞} , O_{L^∞} of density, and normalised CPU cost (normalised with respect to the CPU time taken for the equivalent unlimited scheme at the same grid resolution) for the 2D vortex evolution test problem at the final time of $t = 10$ obtained with the CWENO schemes using various spatial order of accuracy approximations ranging from 3rd-($\mathcal{P}2$ Reconstruction Polynomial) to 6th-order ($\mathcal{P}5$ Reconstruction Polynomial), and linear weight λ_1 for the central stencil. It can be noticed the scheme achieves convergence rates close to their theoretical one for all grid resolutions only when the largest value for the central stencil linear weight is used and is approximately 2.4 times more expensive than the equivalent unlimited scheme.

Order/Number of Edges	$\lambda_1 = 10^3$				$\lambda_1 = 10^7$				$\lambda_1 = 10^{15}$				Cost
Triangular Mesh	e_{L^∞}	O_{L^∞}	e_{L^2}	O_{L^2}	e_{L^∞}	O_{L^∞}	e_{L^2}	O_{L^2}	e_{L^∞}	O_{L^∞}	e_{L^2}	O_{L^2}	CPU
$\mathcal{P}2/16$	3.166E-01	-	4.117E-02	-	1.963E-01	-	2.424E-02	-	1.832E-01	-	2.268E-02	-	2.743
$\mathcal{P}2/32$	1.338E-01	1.24	1.467E-02	1.49	4.059E-02	2.27	5.591E-03	2.12	3.477E-02	2.40	5.059E-03	2.16	1.797
$\mathcal{P}2/64$	3.296E-02	2.02	3.256E-03	2.17	7.734E-03	2.39	1.036E-03	2.43	6.088E-03	2.51	9.269E-04	2.45	2.331
$\mathcal{P}2/128$	7.643E-03	2.11	4.475E-04	2.86	7.785E-04	3.31	1.266E-04	3.03	7.862E-04	2.95	1.257E-04	2.88	2.732
$\mathcal{P}3/16$	3.321E-01	-	4.292E-02	-	1.590E-01	-	1.759E-02	-	3.542E-02	-	5.385E-03	-	2.596
$\mathcal{P}3/32$	1.486E-01	1.16	1.538E-02	1.48	3.492E-02	2.19	3.946E-03	2.16	9.499E-03	1.90	8.616E-04	2.64	2.822
$\mathcal{P}3/64$	5.092E-02	1.55	5.508E-03	1.48	1.316E-02	1.41	7.735E-04	2.35	3.921E-04	4.60	4.784E-05	4.17	2.875
$\mathcal{P}3/128$	1.684E-02	1.60	1.302E-03	2.08	1.321E-03	3.32	3.898E-05	4.31	2.737E-05	3.84	3.043E-06	3.97	2.621
$\mathcal{P}4/16$	3.389E-01	-	4.416E-02	-	2.324E-01	-	2.833E-02	-	5.209E-02	-	6.778E-03	-	2.561
$\mathcal{P}4/32$	1.445E-01	1.23	1.640E-02	1.43	8.291E-02	1.49	8.842E-03	1.68	1.578E-02	1.72	1.306E-03	2.38	2.668
$\mathcal{P}4/64$	5.196E-02	1.48	5.381E-03	1.61	1.984E-02	2.06	1.387E-03	2.67	4.206E-04	5.23	6.855E-05	4.25	2.624
$\mathcal{P}4/128$	1.949E-02	1.41	1.405E-03	1.94	8.909E-04	4.48	3.534E-05	5.29	1.510E-05	4.80	2.520E-06	4.77	2.518
$\mathcal{P}5/16$	3.472E-01	-	4.551E-02	-	2.760E-01	-	3.627E-02	-	5.605E-02	-	4.949E-03	-	2.939
$\mathcal{P}5/32$	1.590E-01	1.13	1.861E-02	1.29	1.193E-01	1.21	1.252E-02	1.53	2.413E-03	4.54	3.107E-04	3.99	2.325
$\mathcal{P}5/64$	6.346E-02	1.32	6.274E-03	1.57	4.412E-02	1.44	3.949E-03	1.66	7.198E-05	5.07	8.041E-06	5.27	2.404
$\mathcal{P}5/128$	2.502E-02	1.34	2.003E-03	1.65	9.912E-03	2.15	5.227E-04	2.92	1.672E-06	5.43	4.616E-07	4.12	2.354
Hybrid Mesh	e_{L^∞}	O_{L^∞}	e_{L^2}	O_{L^2}	e_{L^∞}	O_{L^∞}	e_{L^2}	O_{L^2}	e_{L^∞}	O_{L^∞}	e_{L^2}	O_{L^2}	CPU
$\mathcal{P}2/16$	3.775E-01	-	5.253E-02	-	3.101E-01	-	4.077E-02	-	2.825E-01	-	3.615E-02	-	2.859
$\mathcal{P}2/32$	2.260E-01	0.74	2.694E-02	0.96	9.416E-02	1.72	1.102E-02	1.89	7.682E-02	1.88	1.009E-02	1.84	3.880
$\mathcal{P}2/64$	6.290E-02	1.85	6.829E-03	1.98	1.809E-02	2.38	2.164E-03	2.35	1.271E-02	2.60	1.877E-03	2.43	3.303
$\mathcal{P}2/128$	1.867E-02	1.75	1.345E-03	2.34	2.207E-03	3.04	2.873E-04	2.91	1.891E-03	2.75	2.767E-04	2.76	2.764
$\mathcal{P}3/16$	3.837E-01	-	5.367E-02	-	2.748E-01	-	3.736E-02	-	1.012E-01	-	1.332E-02	-	2.676
$\mathcal{P}3/32$	2.415E-01	0.67	2.857E-02	0.91	9.248E-02	1.57	1.103E-02	1.76	2.924E-02	1.79	2.426E-03	2.46	3.020
$\mathcal{P}3/64$	7.839E-02	1.62	8.142E-03	1.81	3.173E-02	1.54	2.198E-03	2.33	9.806E-04	4.90	1.499E-04	4.02	3.057
$\mathcal{P}3/128$	3.065E-02	1.35	2.884E-03	1.50	3.311E-03	3.26	2.012E-04	3.45	6.475E-05	3.92	7.436E-06	4.33	2.587
$\mathcal{P}4/16$	3.880E-01	-	5.443E-02	-	3.302E-01	-	4.446E-02	-	1.291E-01	-	1.552E-02	-	2.769
$\mathcal{P}4/32$	2.470E-01	0.65	3.099E-02	0.81	1.494E-01	1.14	1.584E-02	1.49	3.056E-02	2.08	2.670E-03	2.54	2.817
$\mathcal{P}4/64$	8.488E-02	1.54	8.766E-03	1.82	4.024E-02	1.89	3.605E-03	2.14	9.727E-04	4.97	1.604E-04	4.06	2.763
$\mathcal{P}4/128$	3.417E-02	1.31	3.224E-03	1.44	3.576E-03	3.49	2.926E-04	3.62	4.189E-05	4.54	6.424E-06	4.64	2.445
$\mathcal{P}5/16$	3.915E-01	-	5.493E-02	-	3.600E-01	-	4.940E-02	-	3.820E-02	-	7.712E-03	-	2.313
$\mathcal{P}5/32$	2.639E-01	0.57	3.389E-02	0.70	2.020E-01	0.83	2.207E-02	1.16	1.337E-02	1.51	1.066E-03	2.86	2.490
$\mathcal{P}5/64$	9.875E-02	1.42	9.921E-03	1.77	6.608E-02	1.61	6.921E-03	1.67	8.712E-04	3.94	4.394E-05	4.60	2.575
$\mathcal{P}5/128$	3.759E-02	1.39	3.959E-03	1.33	1.869E-02	1.82	1.625E-03	2.09	3.966E-06	7.78	6.381E-07	6.11	2.339

on a computational domain given by $[0, 1]^2$ with periodic boundary conditions applied on all sides. The velocity $\mathbf{v}$ describing the revolution of the profile around the centre of the domain $(0.5, 0.5)$ is given by:

$$\mathbf{v}(x, y) = (0.5 - y, x - 0.5). \tag{37}$$

In this particular test three bodies are considered namely a smooth centered at $(x_0 = 0.25, y_0 = 0.5)$, a sharp cone centered at $(x_0 = 0.5, y_0 = 0.25)$ and a slotted cylinder centered at $(x_0 = 0.5, y_0 = 0.75)$ described by the following functions respectively:

$$\mathbf{f}(x, y) = \frac{1 + cos(\pi r(x, y))}{4}, \tag{38}$$

$$\mathbf{f}(x, y) = 1 - r(x, y), \tag{39}$$

and

$$\mathbf{f}(x, y) = \begin{cases} 1, & \text{if } |x - x_0| \geq 0.025 \text{ or y} \geq 0.85 \\ 0, & \text{if otherwise.} \end{cases} \tag{40}$$

Table 4: e_{L^∞} and e_{L^2} error, convergence rates O_{L^∞} , O_{L^∞} of density, and normalised CPU cost (normalised with respect to the CPU time taken for the equivalent unlimited scheme at the same grid resolution) for the 2D vortex evolution test problem at the final time of $t = 10$ obtained with the CWENOZ schemes using various spatial order of accuracy approximations ranging from 3rd-($\mathcal{P}2$ Reconstruction Polynomial) to 6th-order ($\mathcal{P}5$ Reconstruction Polynomial), and linear weight λ_1 for the central stencil. It can be noticed the scheme achieves convergence rates close to their theoretical while not being significantly influenced by the central stencil linear weight value, and is approximately 2.4 times more expensive than the equivalent unlimited scheme.

Order/Number of Edges	$\lambda_1 = 0.9$				$\lambda_1 = 0.999$				$\lambda_1 = 0.999999$				Cost
Triangular Mesh	e_{L^∞}	O_{L^∞}	e_{L^2}	O_{L^2}	e_{L^∞}	O_{L^∞}	e_{L^2}	O_{L^2}	e_{L^∞}	O_{L^∞}	e_{L^2}	O_{L^2}	CPU
$\mathcal{P}2/16$	1.779E-01	-	2.174E-02	-	1.829E-01	-	2.264E-02	-	1.830E-01	-	2.266E-02	-	2.676
$\mathcal{P}2/32$	3.475E-02	2.36	5.055E-03	2.10	3.478E-02	2.40	5.057E-03	2.16	3.478E-02	2.40	5.057E-03	2.16	1.791
$\mathcal{P}2/64$	6.089E-03	2.51	9.271E-04	2.45	6.089E-03	2.51	9.271E-04	2.45	6.089E-03	2.51	9.271E-04	2.45	2.192
$\mathcal{P}2/128$	7.862E-04	2.95	1.257E-04	2.88	7.862E-04	2.95	1.257E-04	2.88	7.862E-04	2.95	1.257E-04	2.88	2.624
$\mathcal{P}3/16$	2.018E-01	-	1.868E-02	-	3.507E-02	-	5.272E-03	-	3.559E-02	-	5.361E-03	-	2.567
$\mathcal{P}3/32$	9.936E-03	4.34	8.703E-04	4.42	9.400E-03	1.90	8.549E-04	2.62	9.397E-03	1.92	8.548E-04	2.65	2.733
$\mathcal{P}3/64$	3.942E-04	4.66	4.827E-05	4.17	3.942E-04	4.58	4.827E-05	4.15	3.942E-04	4.58	4.827E-05	4.15	2.558
$\mathcal{P}3/128$	2.737E-05	3.85	3.043E-06	3.99	2.737E-05	3.85	3.043E-06	3.99	2.737E-05	3.85	3.043E-06	3.99	2.530
$\mathcal{P}4/16$	1.449E-01	-	1.760E-02	-	4.806E-02	-	5.915E-03	-	5.124E-02	-	6.720E-03	-	2.471
$\mathcal{P}4/32$	1.716E-02	3.08	1.338E-03	3.72	1.559E-02	1.62	1.290E-03	2.20	1.557E-02	1.72	1.290E-03	2.38	2.428
$\mathcal{P}4/64$	4.223E-04	5.34	6.881E-05	4.28	4.223E-04	5.21	6.881E-05	4.23	4.223E-04	5.20	6.881E-05	4.23	2.440
$\mathcal{P}4/128$	1.510E-05	4.81	2.520E-06	4.77	1.510E-05	4.81	2.520E-06	4.77	1.510E-05	4.81	2.520E-06	4.77	2.373
$\mathcal{P}5/16$	9.085E-02	-	1.943E-02	-	8.923E-02	-	7.104E-03	-	5.540E-02	-	4.804E-03	-	2.451
$\mathcal{P}5/32$	3.099E-03	4.87	3.143E-04	5.95	2.233E-03	5.32	2.925E-04	4.60	2.229E-03	4.64	2.930E-04	4.04	2.254
$\mathcal{P}5/64$	7.699E-05	5.33	8.410E-06	5.22	7.700E-05	4.86	8.411E-06	5.12	7.700E-05	4.86	8.411E-06	5.12	2.308
$\mathcal{P}5/128$	1.672E-06	5.53	4.616E-07	4.19	1.672E-06	5.53	4.616E-07	4.19	1.672E-06	5.53	4.616E-07	4.19	2.306
Hybrid Mesh	e_{L^∞}	O_{L^∞}	e_{L^2}	O_{L^2}	e_{L^∞}	O_{L^∞}	e_{L^2}	O_{L^2}	e_{L^∞}	O_{L^∞}	e_{L^2}	O_{L^2}	CPU
$\mathcal{P}2/16$	2.720E-01	-	3.436E-02	-	2.823E-01	-	3.611E-02	-	2.828E-01	-	3.620E-02	-	3.456
$\mathcal{P}2/32$	7.631E-02	1.83	9.980E-03	1.78	7.661E-02	1.88	1.008E-02	1.84	7.661E-02	1.88	1.008E-02	1.84	3.244
$\mathcal{P}2/64$	1.268E-02	2.59	1.878E-03	2.41	1.268E-02	2.60	1.878E-03	2.42	1.268E-02	2.60	1.878E-03	2.42	3.184
$\mathcal{P}2/128$	1.891E-03	2.75	2.767E-04	2.76	1.891E-03	2.74	2.767E-04	2.76	1.891E-03	2.74	2.767E-04	2.76	2.737
$\mathcal{P}3/16$	9.570E-02	-	1.697E-02	-	9.008E-02	-	1.186E-02	-	1.035E-01	-	1.363E-02	-	3.323
$\mathcal{P}3/32$	5.191E-02	0.88	3.871E-03	2.13	2.968E-02	1.60	2.469E-03	2.26	2.932E-02	1.82	2.450E-03	2.48	2.977
$\mathcal{P}3/64$	9.206E-04	5.82	1.488E-04	4.70	9.213E-04	5.01	1.489E-04	4.05	9.213E-04	4.99	1.489E-04	4.04	2.943
$\mathcal{P}3/128$	6.475E-05	3.83	7.436E-06	4.32	6.475E-05	3.83	7.436E-06	4.32	6.475E-05	3.83	7.436E-06	4.32	2.577
$\mathcal{P}4/16$	1.353E-01	-	2.077E-02	-	1.136E-01	-	1.397E-02	-	1.347E-01	-	1.630E-02	-	2.873
$\mathcal{P}4/32$	7.738E-02	0.81	5.394E-03	1.94	3.167E-02	1.84	2.757E-03	2.34	2.992E-02	2.17	2.703E-03	2.59	2.761
$\mathcal{P}4/64$	1.010E-03	6.26	1.598E-04	5.08	1.011E-03	4.97	1.599E-04	4.11	1.011E-03	4.89	1.599E-04	4.08	2.752
$\mathcal{P}4/128$	4.188E-05	4.59	6.426E-06	4.64	4.188E-05	4.59	6.426E-06	4.64	4.188E-05	4.59	6.426E-06	4.64	2.437
$\mathcal{P}5/16$	1.872E-01	-	2.655E-02	-	5.940E-02	-	1.192E-02	-	4.354E-02	-	6.389E-03	-	2.343
$\mathcal{P}5/32$	9.904E-02	0.92	7.801E-03	1.77	1.471E-02	2.01	1.084E-03	3.46	1.358E-02	1.68	1.019E-03	2.65	2.476
$\mathcal{P}5/64$	2.300E-04	8.75	2.548E-05	8.26	2.307E-04	5.99	2.566E-05	5.40	2.307E-04	5.88	2.566E-05	5.31	2.526
$\mathcal{P}5/128$	3.946E-06	5.86	6.382E-07	5.32	3.946E-06	5.87	6.382E-07	5.33	3.946E-06	5.87	6.382E-07	5.33	2.336

Where the normalised distance from the centres (x_0, y_0) is given by:

$$r(x, y) = (1/r_0)\sqrt{(x - x_0)^2 + (y - y_0)^2}, \tag{41}$$

with $r_0 = 0.15$. The rest of the domain the solution is initialised with zero, and after one full revolution $t_f = 2\pi$ the exact solution coincides with the initial solution. A triangular unstructured mesh is used as shown in Fig. 3 with 64 edges per side of the computational domain. The WENO, CWENO and CWENOZ schemes ranging from 3rd- to 6th-order of spatial accuracy are employed, with their selected weights from the previous study. The obtained results following one revolution are illustrated in Fig. 4.

From the obtained results it can be noticed that all schemes capture the correct shapes but oscillations in the solutions are present. The CWENO scheme results exhibit smaller oscillations compared to the other schemes while being accurate at smooth extrema. Overall the WENO and CWENOZ schemes are susceptible to larger oscillations in particular at the base of the slotted cylinder, while the CWENO being more dissipative at the top of the slotted cylinder.

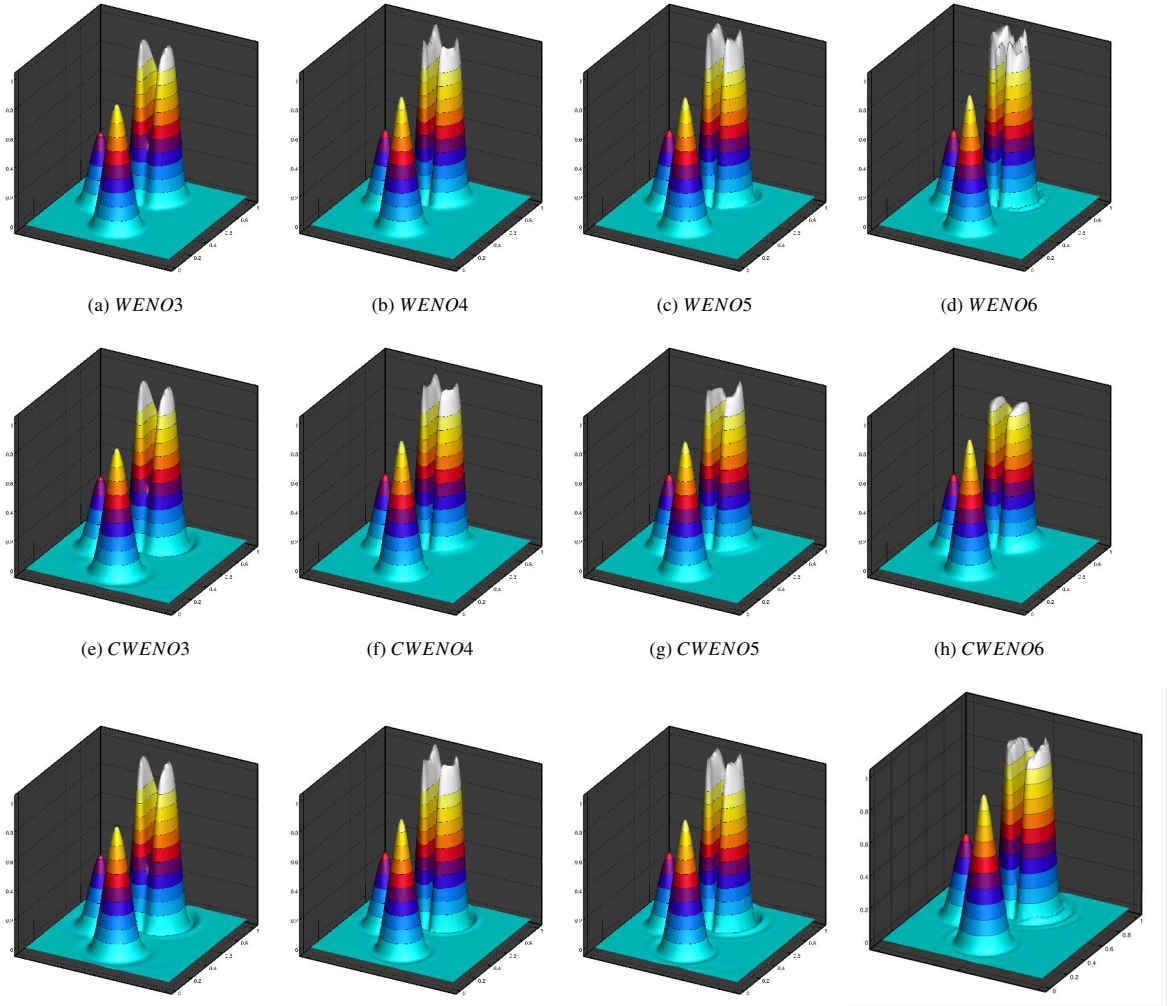

(a) *WENO*3 (b) *WENO*4 (c) *WENO*5 (d) *WENO*6

(e) *CWENO*3 (f) *CWENO*4 (g) *CWENO*5 (h) *CWENO*6

(i) *CWENOZ*3 (j) *CWENOZ*4 (k) *CWENOZ*5 (l) *CWENOZ*6

Figure 4: Computed results after one revolution ($t = 2\pi$) of the solid body rotation test problem, with all the schemes. Three-dimensional elevations of the solution coloured by ten uniformly distributed isolines from 0.1 to 1.0. It can be noticed that all schemes capture the correct shapes but oscillations in the solutions are present. The CWENO scheme results exhibit smaller oscillations compared to the other schemes, in particular at the base of the slotted cylinder.

3.3. Shu-Osher Problem

The well established Shu-Osher [104] test problem is employed, which involves the interaction between a shock wave and an entropy wave. The computational domain is $[-4.5, 4.5] \times [0, 1]$, with periodic boundary conditions in y-axis, a supersonic inflow and outflow on the left and right side of the domain respectively. The initial profile consists of a shock wave $(\rho, u, v, p) = (3.857143, 2.629369, 0, 10.333333)$ on the left when $x < -4$ and an entropy wave in the rest of the domain $(\rho, u, v, p) = (1 + 0.2sin(5x), 0, 0, 1)$.

A 2D triangular mesh is utilised with a resolution of each edge being $h = 0.025$ with approximately $33,886$ elements. The reference solution is computed with a one-dimensional solver of the Euler equations using $10,000$ grid points and employing a 5th order WENO scheme. The calculation is run until $t = 1.8$.

From the density distribution plots shown in Fig. 5 it can be noticed that all the schemes achieve a good agreement with the reference solution, however the WENO 4th-order scheme exhibits a small overprediction of the peaks and valleys at the shock-wave entropy interaction region as also noticed at a smaller extent for CWENO 5th-order scheme. It needs to be highlighted that switching to a higher order CWENO of CWENOZ schemes is considerably cheaper in terms of computational resources compared to the WENO schemes as presented in Table 5. Overall the CWENO and CWENOZ provide a small positive difference compared to the traditional WENO schemes.

Table 5: Normalised computational times (with respect to WENO3) for the Shu-Osher [104] shock tube test problem.

Polynomial Order	WENO	CWENO	CWENOZ
$\mathcal{P}2$	1.00	1.00	0.93
$\mathcal{P}3$	1.44	1.20	1.21
$\mathcal{P}4$	2.25	1.52	1.60

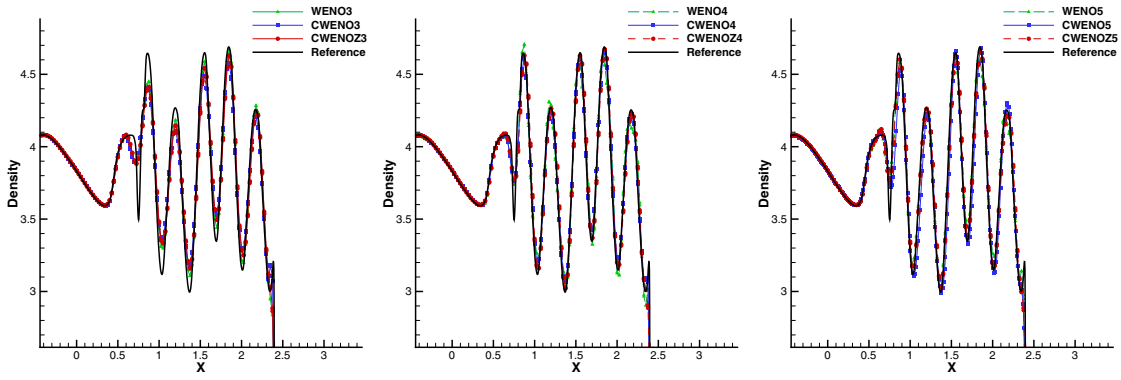

(a) $\mathcal{P}2$ (b) $\mathcal{P}2$ (c) $\mathcal{P}2$

Figure 5: Density distribution for the Shu-Osher [104] shock tube test problem at the final time $t = 1.8$ using various schemes and comparison with the reference solution obtained from the one-dimensional Euler equations on $10,000$ grid points using a WENO-5th order scheme. It can be noticed that the CWENO and CWENOZ are slightly less oscillatory compared to the WENO scheme.

3.4. 2D Riemann Problem

The 2D Riemann problem introduced by Schulz et al. [105] is used, where the computational domain is $[-0.5, 0.5]\times[-0.5, 0.5]$ and the initial condition is given by four different states assigned to each of the quadrants of the domain as shown in Fig. 6. The computational domain has been discretised by a uniform quadrilateral mesh of $400x400$. The simulation has been performed until $t = 0.5$. The variants of the numerical schemes employed are the 4th-order and 6th-order with the reconstruction carried out in conservative variables, and a 6th-order with the reconstruction carried out in characteristic variables.

From the obtained results in Fig. 7 it can be noticed that the all the schemes predict the correct solution pattern, but the WENO implementation provides significantly more oscillatory results compared to the other implementations. This behaviour is expected since all the reconstruction polynomials are of the same order of accuracy, and when a directional stencil has the largest non-linear weight the resulting solution is expected to produce that compared with the CWENO schemes where their directional stencils are lower-order. The WENO scheme results are also the ones with slightly increased number of small-scale structures, and asymmetry of the resulting solution compared to the other schemes. For all the schemes when the reconstruction is carried out in characteristic variables there is a

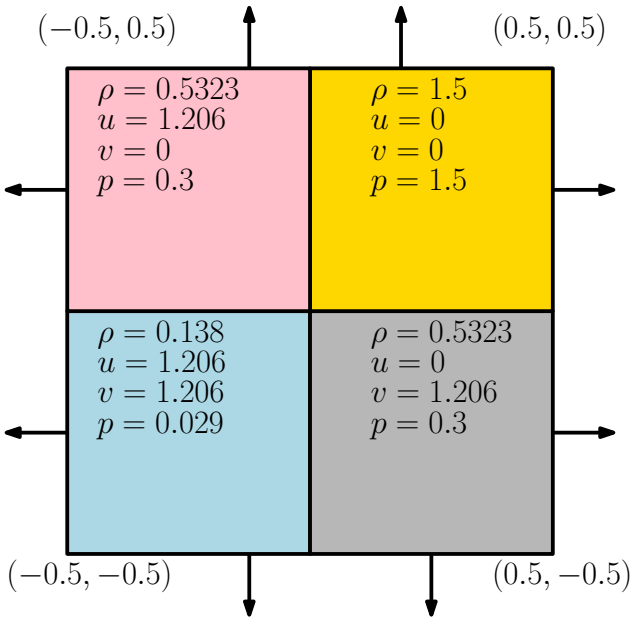

Figure 6: Initial conditions for the multidimensional Riemann problem.

marginal improvement in terms of the roll-ups of the Kelvin-Helmholtz instabilities and the number of structures in the mushroom stem.

.

3.5. ILES of Taylor Green Vortex Re = 1600

The ILES of the 3D viscous Taylor-Green vortex test problem at $Re = 1600$ is employed, for assessing the performance of all the schemes. It is a widely used test problem for the validation of numerical methods, and in particularly at relative coarse-"under-resolved" meshes within the LES context [6, 27, 29, 85, 106–110] due to the pronounced dissipation and dispersion characteristics of non-linear methods. The computational domain is defined as $\Omega = [0, 2\pi]^3$ with periodic boundary conditions. This formulation of the Taylor-Green vortex problem is initialized with the following velocity, density and pressure fields:

$$u(x, y, z, 0) = \sin(kx)\cos(ky)\cos(kz), \tag{42}$$

$$v(x, y, z, 0) = -\cos(kx)\sin(ky)\cos(kz), \tag{43}$$

$$w(x, y, z, 0) = 0, \tag{44}$$

$$\rho(x, y, z, 0) = 1, \tag{45}$$

$$p(x, y, z, 0) = 100 + \frac{\rho}{16}[\cos(2z) + 2] \cdot [\cos(2x) + \cos(2y)]. \tag{46}$$

The initial condition corresponds to an initial Mach number $M \approx 0.08$, with wavenumber $k = 2\pi/\lambda = 1$. Simulations were carried out on a hexahedral mesh of 96^3 and 128^3 resolution with 4th-order and 5th-order spatial discretisation schemes respectively. The WENO, CWENO, and CWENOZ variants were used with a CFL number of 1.3 for the explicit Runge-Kutta 4th-order scheme, up to $t = 20$ for obtaining the dissipation statistics. The DNS

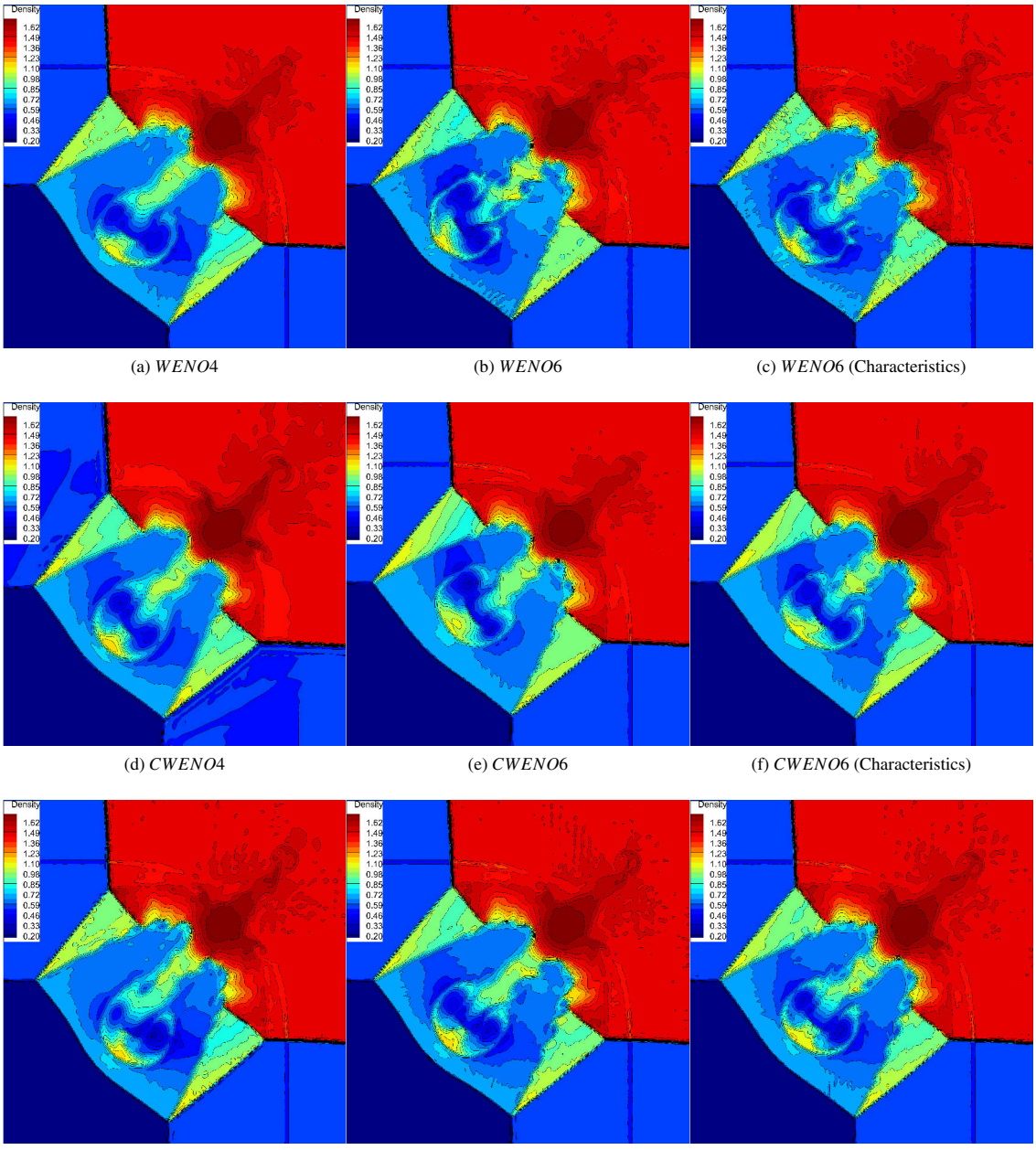

(a) $WENO4$ (b) $WENO6$ (c) $WENO6$ (Characteristics)

(d) $CWENO4$ (e) $CWENO6$ (f) $CWENO6$ (Characteristics)

(g) $CWENOZ4$ (h) $CWENOZ6$ (i) $CWENOZ6$ (Characteristics)

Figure 7: Density distribution with various 4th-order numerical schemes for the multidimensional Riemann problem at $t_{final} = 1.0$. Only the lower left portion of the computational domain is shown. It can be noticed that the all the schemes predict the correct solution pattern, but the WENO implementation provides significantly more oscillatory results and a more pronounced loss of symmetry compared to the other implementations.

results of Brachet et. al [111] are used for comparisons against the computed solutions. For numerical results for the 3D Taylor-Green vortex obtained with a new family of staggered semi-implicit discontinuous Galerkin finite element

schemes, see [112–115].

From the obtained results as shown in Fig. 9 it can be seen that the energy dissipation rate for all the 4th-order schemes is within the $Re = 800 - 1600$ DNS results range, as the we move to the 5th-order schemes with a finer mesh the agreement with the $Re = 1600$ DNS results improves as expected. The structure predicted near $t \approx= 5 - 6$ for the 5th-order scheme are due to the specific aspects of the ILES framework of the schemes, and are present in multidimensional numerical methods as previously reported in the previous studies by Drikakis et al. [106].The key differences between the CWENO and CWENOZ schemes is a slightly larger secondary peak at $t = 9.5$ for the 96^3 resolution, and an earlier peak for the CWENOZ scheme for the 128^3 resolution, whereas the results from the WENO schemes indicate a more dissipative behaviour for both settings.

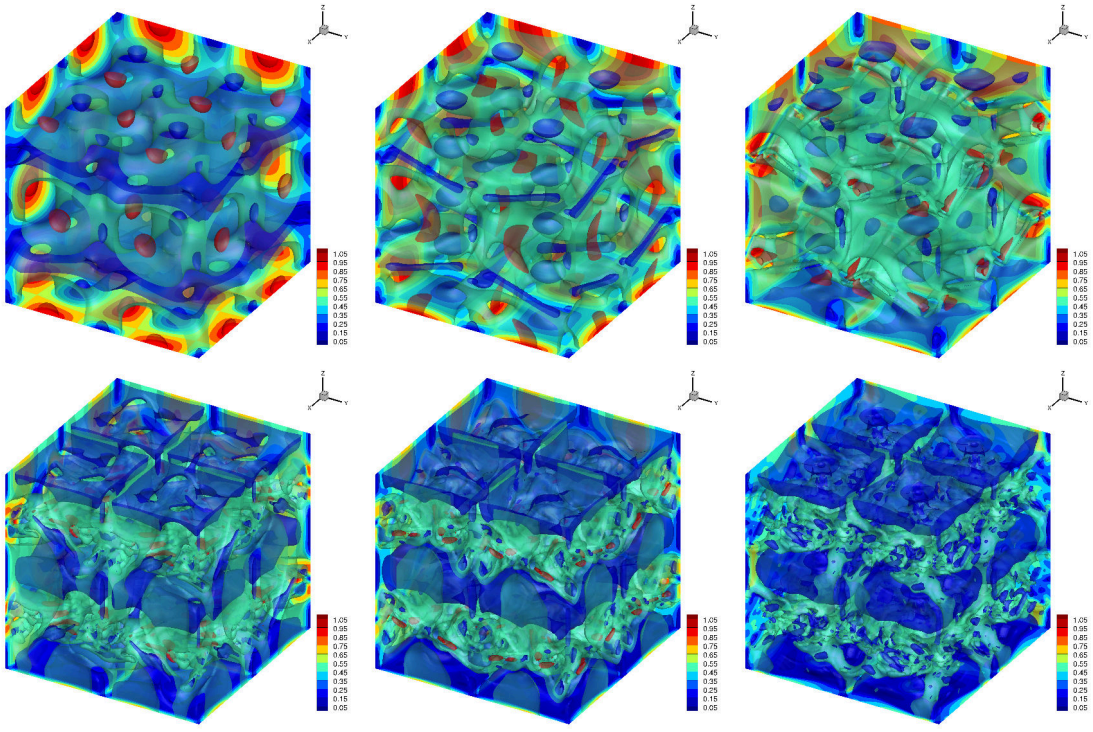

Figure 8: solution of the Taylor-Green vortex flow at Re=1600 computed with the CWENO5 scheme on a hexahedral mesh of 128^3. The isosurfaces of the velocity magnitude at three levels $(0.1, 0.5, 1.0)$ are plotted at times $t = 1.3, 2.7, 4.1, 6.4, 8.2$ and 11 from top left to bottom right respectively.

This test problem has been used to assess the computational costs of all the schemes. Ultimately we want to understand the computational savings that the CWENO and CWENOZ schemes can offer compared to the traditional WENO schemes. It needs to be stressed that the key memory requirement for each scheme is dependent of the storage of the Moore-Penrose pseudo-inverse of the matrix A_{mk} of Eq. (14), and this is where the key difference between a CWENO/CWENOZ and WENO schemes lie. For example for each hexahedral cell, for each conserved variable a WENO6 scheme would require approximately 338 kBytes of memory for storage of these matrices, while a CWENO/CWENOZ scheme require just 49kBytes of memory. Therefore significant savings in terms of storage are obtained with CWENO/CWENOZ reduced memory footprint.The communication of the values of for the halo cells arising from directional stencils become important (14% total time per iteration) at partitions of fewer than 160 elements per physical core for a 6th-order scheme as reported by Tsoutsanis et al. [86] for the present implementation of UCNS3D. Therefore the reduction of the size directional stencils for CWENO/CWENOZ schemes would prove beneficial for massively parallel simulations at partitions that include fewer than 160 elements per physical core.

The process involved running each of the schemes for 1000 iterations and averaging the total time taken per

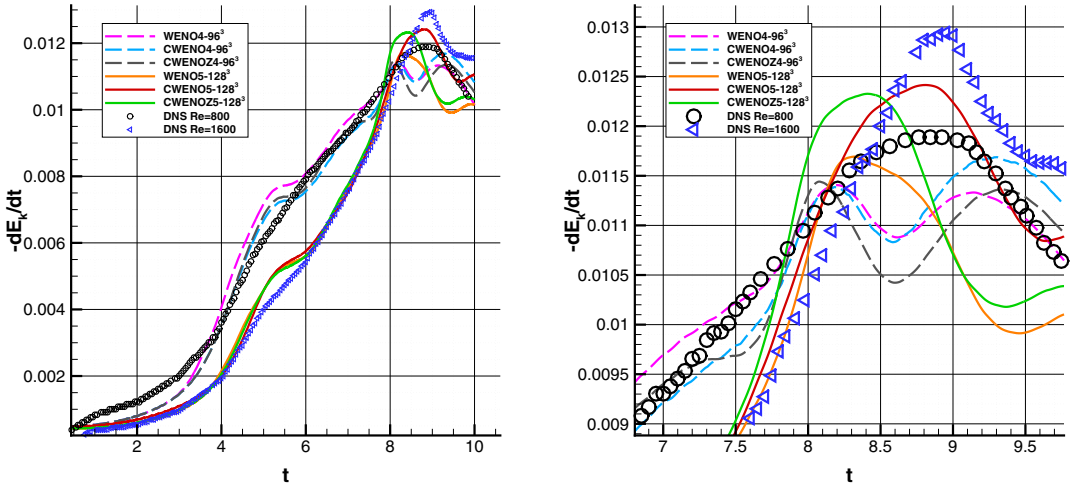

Figure 9: Kinetic energy dissipation rate for the viscous ILES of the Taylor-Green Vortex $Re = 1600$ obtained with various schemes on a 96^3 and 128^3 ‘ hexahedral meshe, and comparison with the DNS results of Brachet et al.[111]. It can be noticed that all the schemes perform similarly, with CWENO and CWENOZ schemes being marginally less dissipative compared to WENO. The WENO4 scheme being 1.36 times more expensive computationally compared to CWENO and CWENOZ. Increasing the order of accuracy and grid resolution a better agreeement with the DNS results is obtained.

iteration while excluding initialisation times, and I/O times. For this purpose, the University of Cambridge Tier-2 national high-performance computing service Peta4 was used, and in particular the Intel Xeon-Knights Landing cluster consisting of 342 nodes of Intel Xeon Phi 7210 with 96GB or RAM and Intel OPA at 100Gbs. All the simulations where exectured with the utilisation of hybrid MPI+OPENMP implementation of the UCNS3D code, with 4 MPI processes per Knights Landing chip, and 64 threads spawned from each one of them, resulting a total of 256 threads per chip. This combination was found to be the ideal combination as thoroughly documented in [86]. All the simulations where executed in 20 Intel Xeon Phi 7210 processors, involving 80 MPI processes and 5,120 threads in total.

As expected the improvements in terms of computational times for the CWENO/CWENOZ schemes compared to WENO schemes become more prominent as the polynomial order is increased as seen in Table 6 at least for the reconstructions with respect to the conservative variables. On the other hand for the reconstruction in characteristic variables the computational cost is increased for all the schemes. But for the central schemes the computational cost increment is larger for WENO scheme when switching from conservative to characteristic variables. This attribute is linked to the additional computations required for the central schemes for the p_1 polynomial according to Eq. (23), since the projection of the polynomial degrees of freedom to characteristic space for the calculation of the WENO weights is the most computational expensive process as reported in [86]. Therefore the characteristic variable reconstruction should be deployed only when really needed due to the increased computational cost.

Since we have not noticed significant differences in terms of accuracy between the current implementation of CWENO and CWENOZ schemes, but a slightly more robust non-oscillatory behaviour from the CWENO family, from this point onward the CWENO scheme will be utilised for the remaining test problems.

3.6. Schardin's Problem

The well established test problem of Schardin [116] is employed to assess the performance of the CWENO scheme, since this test problem involves multiple challenging flow structures interacting such as reflected shocks, Mach stems, contact waves, and vortices. A moving normal shock with Mach number $M_s = 1.34$ is encountering a triangular wedge and the size of the computational domain is similar to the experimental one as seen in Fig. 10.

Table 6: Normalised computational times (with respect to CWENO3) for all the schemes for the viscous ILES of the Taylor-Green Vortex.

Polynomial Order	CWENO/Z (Conservative)	WENO (Conservative)	CWENO/Z (Characteristics)	WENO (Characteristics)
$\mathcal{P}2$	1.00	1.04	2.57	2.52
$\mathcal{P}3$	1.61	2.19	3.80	4.04
$\mathcal{P}4$	2.76	3.84	5.90	6.46
$\mathcal{P}5$	4.80	7.04	9.09	10.28

Table 7: Initial Conditions for Schardin's test problem

Parameter	Post-Shock	Pre-Shock
P (Pa)	195557.25	101325
T (K)	350.5	288.15
$\mathbf{u}(m/s)$	(168.62,0,0)	(0,0,0)

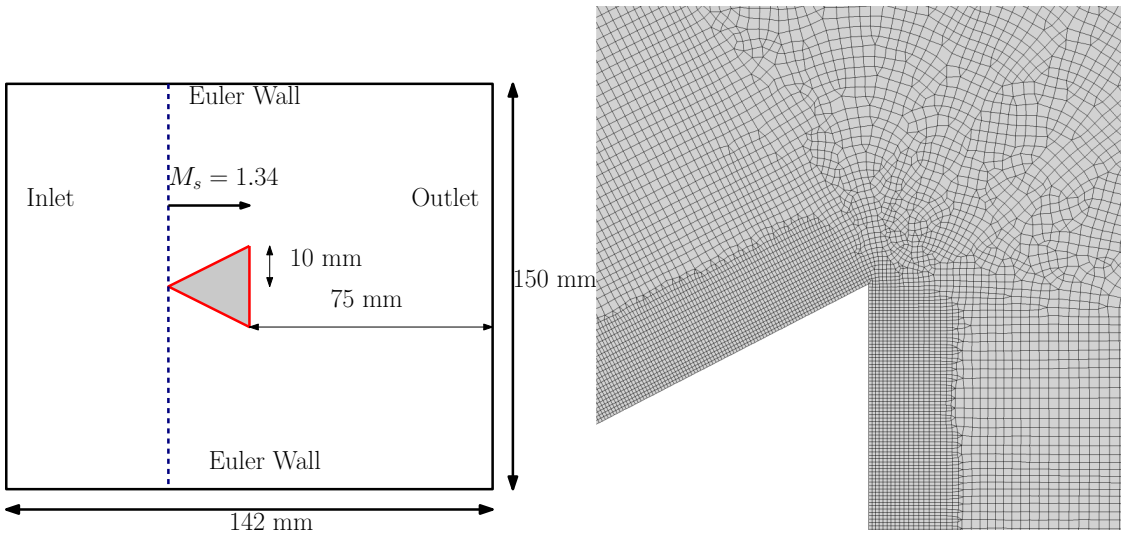

(a) Computational domain

(b) Mesh

Figure 10: Computational domain with boundary conditions, and blown-up view of the mesh close to the triangular wedge for the Schardin's test problem.

The initial conditions are listed in Table 7, additionaly the gas constant is $R = 287 J/kg \cdot K$, and the ratio of specific heats $\gamma = 1.4$. The hybrid computational mesh employed can be seen in Fig. 10 and consists of $5,264,594$ cells with a resolution of $h = 0.01mm$ close to the wall, the prescribed boundary conditions correspond to a supersonic inflow and outflow, with inviscid wall boundary condition applied for the triangular wedge and the top and bottom sides of the domain as seen in Fig. 10. The inviscid Euler equations are solved with a CWENO5 scheme using characteristic variables reconstruction with a 4th-order (SSP) Runge-Kutta time stepping scheme while using $CFL = 1.4$. At the start time $t = 0$ the incident shock wave contacts the triangular wedge, and the simulation is run for $t = 200ms$. The obtained results are compared with the experimental imaging of Chang and Chang [117] at different instants as it can be seen in Fig. 11. From the results it can be noticed that all the flow features of the experiment are captured

at their correct location such as as the bow shock, tip vortices, contact surfaces between the tip vortices and the shock triple point. The combination of the relatively fine mesh, and the CWENO5 is sufficient to capture the acoustic waves produced by the shock-vortexlet interactions as shown in Fig. 12, and agreeing with the experimental and computational results of Chang and Chang [117]. Finally the prediction of the Mach number along the symmetry line at the wake of the triangular wedge agrees well with the results of of Chang and Chang [117] as seen in Fig. 12.

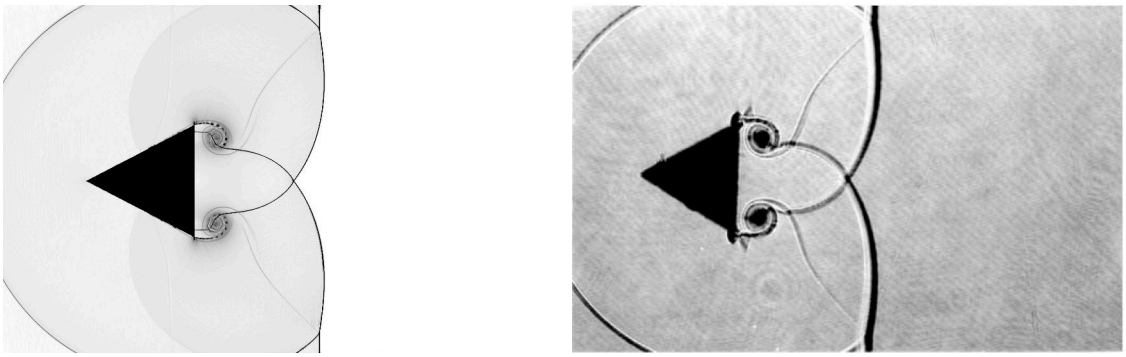

(a) $t = 91ms$

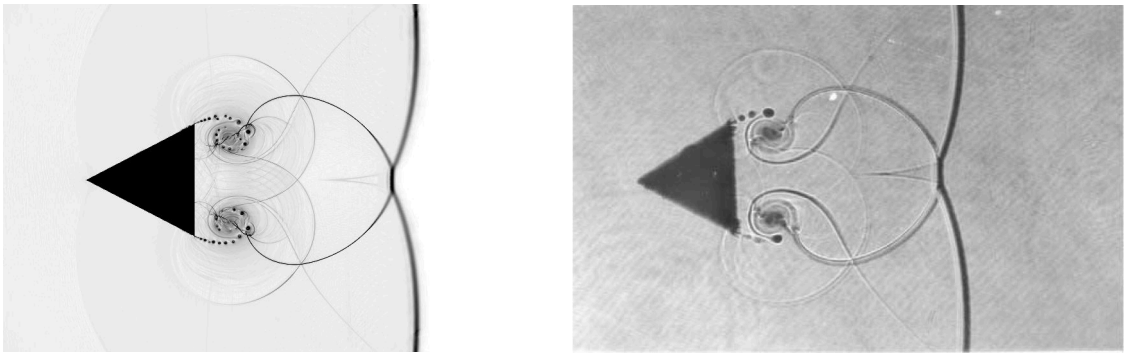

(b) $t = 128ms$

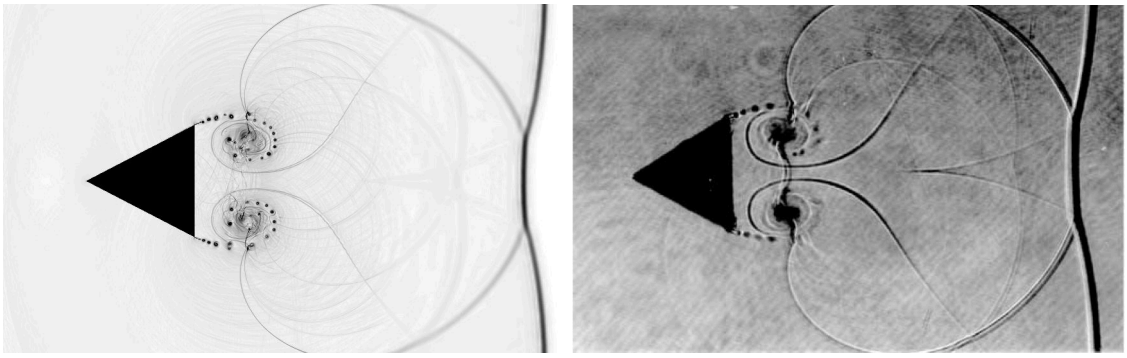

(c) $t = 178ms$

Figure 11: Contour plots of density gradient magnitude for the Schardin's test problem at various instants as computed with the present CWENO5 scheme (left), and comparison with the experimental results of Chang and Chang [117] (right)

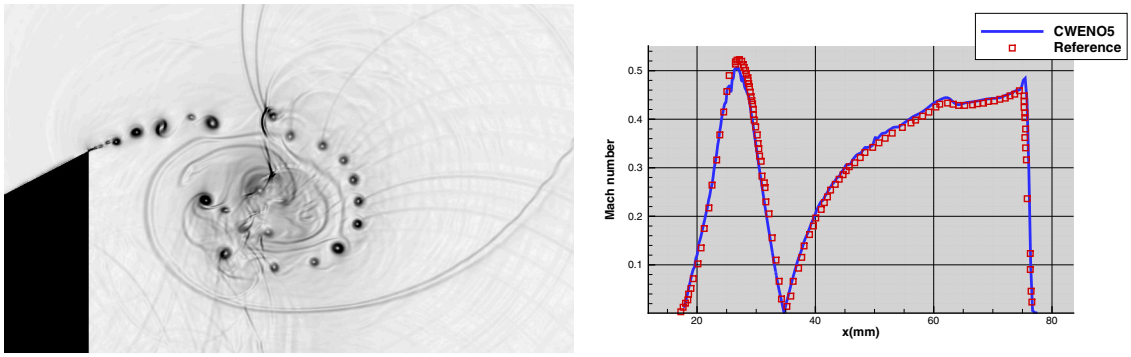

(a) contour plots of the density gradient magnitude

(b) Mach number variation

Figure 12: Contour plots of the density gradient magnitude for Schardin's test problem at the shock-vortexlet interaction zone at $t = 172ms$ (left), and Mach number variation at the symmetry line wake of the triangular wedge and comparison with the results of Chang and Chang [117] (right).

3.7. ILES of Transonic cylinder Re = 3900

The last test case concerns the ILES of a transonic infinite cylinder of diameter $D = 1$ at $Re = 3900$ and $M_\infty = 0.8$. The majority of the available computational studies are focused on the subsonic ($M_\infty = 0.2$) regime for this Reynolds number [29, 118–125] for subsonic Mach numbers. However, beyond $M_\infty = 0.75$ a multitude of phenomena occur including shock wave boundary layer, shock wave shear layer and shocklet/turbulence interaction, forming an ideal environment for assessing the robustness and fidelity of the developed schemes.

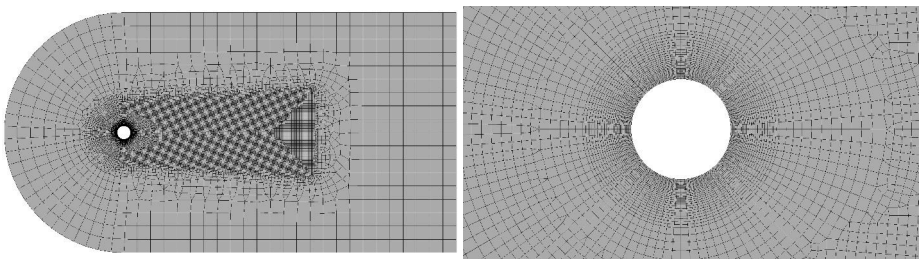

Figure 13: Overview of the hybrid unstructured mesh used for the transonic flow past an infinite cylinder at $Re = 3900$ and $M_\infty = 0.8$.

For this case a very coarse hybrid unstructured mesh of approximately 0.8 million cells is used, consisting of hexahedral and prismatic cells as illustrated in Fig. 13. The domain extends $10D$ upstream and $25D$ downstream, and $\pi \cdot D$ in the z-direction. The grid resolution at the boundary layer region gives a $y^+ \approx 1$ at the first cell-centre off the surface, 64 cells are used in the z-direction, and a refinement region at the wake of the cylinder is used for $10D$ downstream with an average cell length of 0.09. Periodic boundary conditions are used in the z-direction, no-slip boundary conditions at the surface of the cylinder and free-stream conditions at the farfield. The CWENO 4th-order scheme is used, with a CFL number of 1.45. The simulation was run for $t = 50t_c$ where $t_c = D/U_\infty$ for the initial transients to settle, and for an additional $240t_c$ for obtaining sufficiently converged statistical data. The variation of lift and drag coefficient can be seen in Fig. 14, with the averaged drag coefficient from this study being within the range of results provided by previous computational studies, experiments and flight test as listed in Table 8 at the same Mach number, although the Reynolds number is not the same.

From the time-averaged and spanwise-averaged pressure coefficient obtained as seen in Fig. 15 the results obtained are in reasonable agreement with the computational results of Xia et al. [126] $Re = 4\times10^4$ (CLES) in terms of pressure coefficient up until 70 °. Beyond that the separation and reattachment occur at different locations as seen from the skin friction coefficient, which is mainly attributed to the different Reynolds number. From the instantaneous flow-field

Table 8: Comparison of drag coefficient with experimental and computational results at Mach=0.8

Source	C_D
Present CWENO4 (ILES)	1.408
Xia et al.[126] $Re = 4 \times 10^4$ (CLES)	1.353
Xia et al.[126] $Re = 1 \times 10^6$ (CLES)	1.312
Welsh [127] (Flight Test)	1.425
Macha [128] (Experiment)	1.529

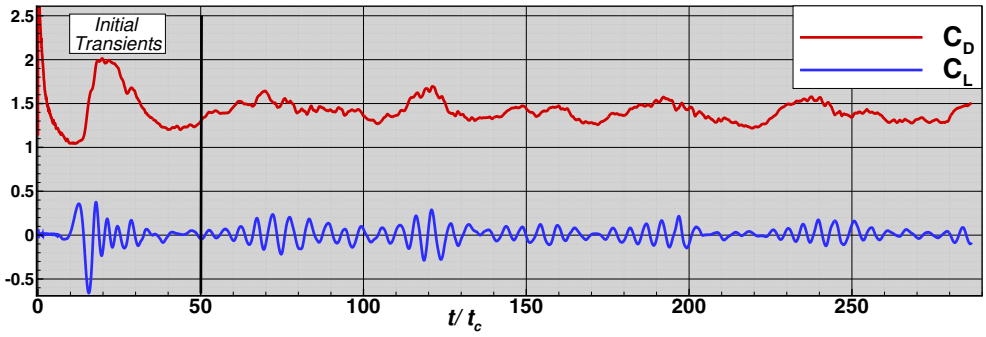

Figure 14: Lift and drag coefficients variations in time for the flow past a cylinder at $Re = 3900$ and $M_\infty = 0.8$.

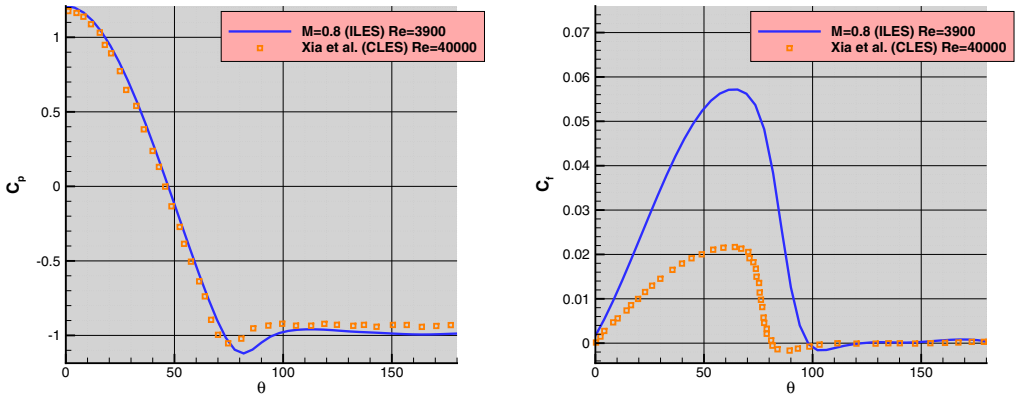

Figure 15: Time-averaged and spanwise-averaged pressure coefficient and skin friction coefficient for the for the flow past a cylinder at $Re = 3900$ and $M_\infty = 0.8$ and comparison with the results of Xia et al.[126] $Re = 4 \times 10^4$ and $M_\infty = 0.8$ (CLES).

solution as seen in Fig. 16 it can be noticed that all the flow features typical of this regime such as the shocks at the shoulders of the cylinder, and the long shear layers interaction with the shocklets at the near wake agree with previous studies of Xia et al. [126] .

Finally, by placing probes at different locations in the wake of the cylinder the dominant vortex shedding frequency was found to be $St = 0.185$ as seen in Fig. 17, which is lower compared to the subsonic case of $M_\infty = 0.2$ for the same Reynolds number as reported in [29, 118–125], but agrees well with the trends noticed in previous experimental

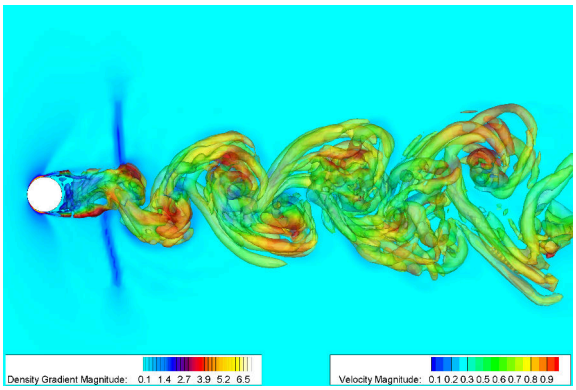

Figure 16: Isosurfaces of Q-criterion coloured by velocity magnitude, and contour plots of the density gradient magnitude on a 2D slice at z=0, for the flow past a cylinder at $Re = 3900$ and $M_\infty = 0.8$, where the interaction of the vortical structures with shock waves typical of this flow regime can be noticed.

and computational studies as reported by Canuto and Taira [129] where the Strouhal number is reduced when Mach number increases.

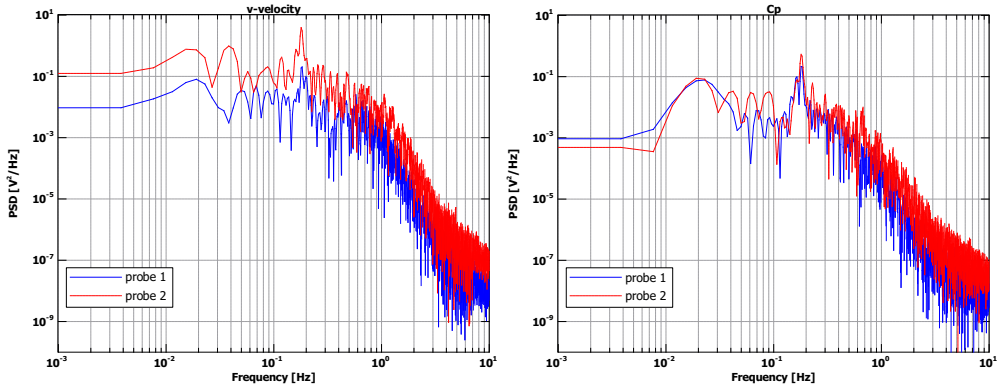

Figure 17: 1D frequency spectra for two probe positions located at (1.30,0.69,$\pi/2$) and (2.0,0.59,$\pi/2$) the transonic flow past an infinite cylinder at $Re = 3900$ and $M_\infty = 0.8$.

4. Conclusions

This paper extends the central high-order non-oscillatory family of schemes to mixed-element unstructured meshes up to 6th-order of spatial accuracy. The performance benefits obtained from the CWENO and CWENOZ class of schemes are not only related to a decreased computational time compared to the WENO schemes but significantly improved robustness. The latter being linked with the compactness of the directional stencils that increase the probability of at least one of them lying in smooth-data regions. The CWENO scheme exhibits an increased sensitivity compared to CWENOZ and WENO with respect to the value of the linear weight assigned to the central stencil, since a large value is required to achieve the designed order of accuracy for mixed-element unstructured meshes. On the other hand the CWENO demonstrated the most robust non-oscillatory behaviour in all the test problems, and was therefore the method of choice for the last two test problems which included a plethora of smooth and discontinuous flow features, where a good agreement with experimental results was obtained.

The computational cost of the new class of schemes can be approximately up to 30% less than the equivalent WENO scheme in 3D when conservative variables reconstruction are used. However, when switching to characteristic variables the cost of the schemes is approximately up to 11% less compared to WENO schemes. For characteristic variables reconstruction the most expensive procedure is the projection of the polynomial degrees of freedom to characteristic space. For the CWENO/CWENOZ schemes the additional operations required by the p_1 polynomial are significantly greater compared to the central stencil polynomial of the WENO schemes. The latter is not considered an important drawback due to the reduced complexity of the algorithm, and the reduced size of the directional stencils that will translate to reduced communications across processes and reduced memory footprint for massively parallel computations .

Expanding the current family of schemes to the targeted ENO schemes [130–132] for further reducing their computational footprint is an interesting line of future research. Future developments will concern the extension of the subject schemes to overset meshes for industrial-scale applications since the compact nature of the present non-oscillatory schemes can be useful for interpolating the solutions across different meshes. Future applications of the method proposed in this paper will concern the unified first order hyperbolic model of continuum mechanics proposed and discussed in [59, 133, 134], as well as the novel first order hyperbolic reformulations of nonlinear dispersive systems forwarded in [135, 136]. With the high order CWENOZ schemes developed in this paper we also plan to study natural convection problems in the low Mach number limit, similar to the problems investigated in [137, 138].

Acknowledgements

The authors acknowledge the computing time on the University of Cambridge Tier-2 national high-performance computing service Peta4 provided through the EPSRC grant EP/P020259/1. The authors also acknowledge the computing time at CINECA (Bologna - IT) provided through the Project HPC-EUROPA3 (INFRAIA-2016-1-730897), with the support of the EC Research Innovation Action under the H2020 Programme and the computing time on ARCHER through UK Turbulence Consortium [EPSRC grant number EP/L000261/1 and EP/R029326/1]. M.D. received financial support from the Italian Ministry of Education, University and Research (MIUR) in the frame of the Departments of Excellence Initiative 2018–2022 attributed to DICAM of the University of Trento (grant L. 232/2016) and in the frame of the PRIN Project 2017 *Innovative numerical methods for evolutionary partial differential equations and applications*. M.D. is member of the INdAM GNCS group.

References

[1] M. Dumbser, W. Boscheri, M. Semplice, G. Russo, Central weighted ENO schemes for hyperbolic conservation laws on fixed and moving unstructured meshes, SIAM Journal on Scientific Computing 39 (6) (2017) A2564–A2591. doi:10.1137/17M1111036.

[2] P. Bakhvalov, T. Kozubskaya, EBR-WENO scheme for solving gas dynamics problems with discontinuities on unstructured meshes, Computers and Fluids 157 (2017) 312–324.

[3] S. Diot, S. Clain, R. Loubére, Improved detection criteria for the multi-dimensional optimal order detection (MOOD) on unstructured meshes with very high-order polynomials, Computers and Fluids 64 (2012) 43–63. doi:10.1016/j.compfluid.2012.05.004.

[4] S. Clain, S. Diot, R. Loubére, A high-order finite volume method for systems of conservation laws-multi-dimensional optimal order detection (MOOD), Journal of Computational Physics 230 (10) (2011) 4028–4050. doi:10.1016/j.jcp.2011.02.026.

[5] P. Tsoutsanis, V. Titarev, D. Drikakis, WENO schemes on arbitrary mixed-element unstructured meshes in three space dimensions, Journal of Computational Physics 230 (4) (2011) 1585–1601.

[6] P. Tsoutsanis, A. Antoniadis, D. Drikakis, WENO schemes on arbitrary unstructured meshes for laminar, transitional and turbulent flows, Journal of Computational Physics 256 (2014) 254–276.

[7] G. Lei, W. Li, Y. Ren, High-order unstructured-grid WENO fvm for compressible flow computation, Jisuan Wuli/Chinese Journal of Computational Physics 28 (5) (2011) 633–640.

[8] W. Li, Y.-X. Ren, High-order k-exact WENO finite volume schemes for solving gas dynamic Euler equations on unstructured grids, International Journal for Numerical Methods in Fluids 70 (6) (2012) 742–763.

[9] G. Hu, R. Li, T. Tang, A robust WENO type finite volume solver for steady Euler equations on unstructured grids, Communications in Computational Physics 9 (3) (2011) 627–648.

[10] H.-S. Zheng, N. Zhao, J. Zhu, High order finite volume weighted essentially non-oscillatory schemes on two dimensional unstructured meshes, Kongqi Donglixue Xuebao/Acta Aerodynamica Sinica 28 (4) (2010) 446–451.

[11] L. Ivan, C. Groth, High-order solution-adaptive central essentially non-oscillatory (CENO) method for viscous flows, Journal of Computational Physics 257 (PA) (2014) 830–862. doi:10.1016/j.jcp.2013.09.045.

[12] D. Levy, S. Nayak, C.-W. Shu, Y.-T. Zhang, Central WENO schemes for hamilton-jacobi equations on triangular meshes, SIAM Journal on Scientific Computing 28 (6) (2006) 2229–2247.

[13] M. Dumbser, M. Kaser, V. Titarev, E. Toro, Quadrature-free non-oscillatory finite volume schemes on unstructured meshes for nonlinear hyperbolic systems, Journal of Computational Physics 226 (1) (2007) 204–243.
[14] M. Dumbser, M. Kaser, Arbitrary high order non-oscillatory finite volume schemes on unstructured meshes for linear hyperbolic systems, Journal of Computational Physics 221 (2) (2007) 693–723.
[15] R. Abgrall, On essentially non-oscillatory schemes on unstructured meshes: analysis and implementation, Journal of Computational Physics 114 (1) (1994) 45–58.
[16] O. Friedrich, Weighted essentially non-oscillatory schemes for the interpolation of mean values on unstructured grids, Journal of Computational Physics 144 (1) (1998) 194–212.
[17] X. Liu, L. Xuan, Y. Xia, H. Luo, A reconstructed discontinuous Galerkin method for the compressible Navier-Stokes equations on three-dimensional hybrid grids, Computers and Fluids 152 (2017) 217–230. doi:10.1016/j.compfluid.2017.04.027.
[18] J. Zhu, J. Qiu, Hermite WENO schemes and their application as limiters for Runge-Kutta Discontinuous Galerkin method, iii: Unstructured meshes, Journal of Scientific Computing 39 (2) (2009) 293–321.
[19] Z. Xu, Y. Liu, C.-W. Shu, Hierarchical reconstruction for Discontinuous Galerkin methods on unstructured grids with a WENO-type linear reconstruction and partial neighboring cells, Journal of Computational Physics 228 (6) (2009) 2194–2212.
[20] M. Dumbser, D. Balsara, E. Toro, C.-D. Munz, A unified framework for the construction of one-step finite volume and Discontinuous Galerkin schemes on unstructured meshes, Journal of Computational Physics 227 (18) (2008) 8209–8253.
[21] J. Zhu, J. Qiu, C.-W. Shu, M. Dumbser, Runge-Kutta Discontinuous Galerkin method using WENO limiters ii: Unstructured meshes, Journal of Computational Physics 227 (9) (2008) 4330–4353.
[22] H. Luo, J. Baum, R. Lohner, A Hermite WENO-based limiter for Discontinuous Galerkin method on unstructured grids, Journal of Computational Physics 225 (1) (2007) 686–713.
[23] X. Zhang, Y. Xia, C.-W. Shu, Maximum-principle-satisfying and positivity-preserving high order Discontinuous Galerkin schemes for conservation laws on triangular meshes, Journal of Scientific Computing (2011) 1–34.
[24] P. Vincent, A. Farrington, F. Witherden, A. Jameson, An extended range of stable-symmetric-conservative flux reconstruction correction functions, Computer Methods in Applied Mechanics and Engineering 296 (2015) 248–272. doi:10.1016/j.cma.2015.07.023.
[25] J. Bull, A. Jameson, High-order flux reconstruction schemes for LES on tetrahedral meshes, Notes on Numerical Fluid Mechanics and Multidisciplinary Design 130 (2015) 69–79.
[26] D. De Grazia, G. Mengaldo, D. Moxey, P. Vincent, S. Sherwin, Connections between the Discontinuous Galerkin method and high-order flux reconstruction schemes, International Journal for Numerical Methods in Fluids 75 (12) (2014) 860–877. doi:10.1002/fld.3915.
[27] J. Bull, A. Jameson, Simulation of the Taylor-Green vortex using high-order flux reconstruction schemes, AIAA Journal 53 (9) (2015) 2750–2761.
[28] D. Williams, P. Castonguay, P. Vincent, A. Jameson, Energy stable flux reconstruction schemes for advection-diffusion problems on triangles, Journal of Computational Physics 250 (2013) 53–76. doi:10.1016/j.jcp.2013.05.007.
[29] B. Vermeire, F. Witherden, P. Vincent, On the utility of GPU accelerated high-order methods for unsteady flow simulations: A comparison with industry-standard tools, Journal of Computational Physics 334 (2017) 497–521.
[30] J. A., P. Vincent, P. Castonguay, On the non-linear stability of flux reconstruction schemes, Journal of Scientific Computing 50 (2) (2012) 434–445. doi:10.1007/s10915-011-9490-6.
[31] P. Castonguay, P. Vincent, A. Jameson, A new class of high-order energy stable flux reconstruction schemes for triangular elements, Journal of Scientific Computing 51 (1) (2012) 224–256. doi:10.1007/s10915-011-9505-3.
[32] C. Breviglieri, A. Maximiliano, E. Basso, J. Azevedo, Improved high-order spectral finite volume method implementation for aerodynamic flows, 27th AIAA Applied Aerodynamics Conference (79128).
[33] Z. Xu, Y. Liu, C.-W. Shu, Hierarchical reconstruction for spectral volume method on unstructured grids, Journal of Computational Physics 228 (16) (2009) 5787–5802.
[34] C.-W. Shu, Tvb uniformly high-order schemes for conservation laws, Mathematics of Computation 49 (179) (1987) 105–121.
[35] M. S. Darwish, F. Moukalled, TVD schemes for unstructured grids, International Journal of Heat and Mass Transfer 46 (4) (2003) 599–611. doi:10.1016/S0017-9310(02)00330-7.
[36] L. Tang, S. Song, A tvd-type method for 2d scalar hamilton-jacobi equations on unstructured meshes, Journal of Computational and Applied Mathematics 195 (1-2) (2006) 182–191.
[37] J. Furst, K. Kozel, Application of second order TVD and WENO schemes in internal aerodynamics, Journal of Scientific Computing 17 (1-4) (2002) 253–262.
[38] P. Tsoutsanis, Extended bounds limiter for high-order finite-volume schemes on unstructured meshes, Journal of Computational Physics 362 (2018) 69–94.
[39] M. Hubbard, Multidimensional slope limiters for muscl-type finite volume schemes on unstructured grids, Journal of Computational Physics 155 (1) (1999) 54–74. doi:10.1006/jcph.1999.6329.
[40] K. Michalak, C. Ollivier-Gooch, Limiters for unstructured higher-order accurate solutions of the Euler equations, 46th AIAA Aerospace Sciences Meeting and Exhibit.
[41] T. Buffard, S. Clain, Monoslope and multislope muscl methods for unstructured meshes, Journal of Computational Physics 229 (10) (2010) 3745–3776. doi:10.1016/j.jcp.2010.01.026.
[42] C. Michalak, C. Ollivier-Gooch, Accuracy preserving limiter for the high-order accurate solution of the Euler equations, Journal of Computational Physics 228 (23) (2009) 8693–8711.
[43] F. Haider, J.-P. Croisille, B. Courbet, Stability analysis of the cell centered finite-volume muscl method on unstructured grids, Numerische Mathematik 113 (4) (2009) 555–600. doi:10.1007/s00211-009-0242-6.
[44] B. van Leer, Towards the ultimate conservative difference scheme. v. a second-order sequel to Godunov's method, Journal of Computational Physics 32 (1) (1979) 101–136.
[45] B. Van Leer, Towards the ultimate conservative difference scheme. iv. a new approach to numerical convection, Journal of Computational Physics 23 (3) (1977) 276–299.

[46] B. van Leer, Towards the ultimate conservative difference scheme. ii. monotonicity and conservation combined in a second-order scheme, Journal of Computational Physics 14 (4) (1974) 361–370.
[47] P. Farmakis, P. Tsoutsanis, X. Nogueira, WENO schemes on unstructured meshes using a relaxed a posteriori MOOD limiting approach, Computer Methods in Applied Mechanics and Engineering 363. doi:10.1016/j.cma.2020.112921.
[48] X. Nogueira, L. Ramirez, J. Fernandez-Fidalgo, M. Deligant, S. Khelladi, J.-C. Chassaing, F. Navarrina, An a posteriori-implicit turbulent model with automatic dissipation adjustment for large eddy simulation of compressible flows, Computers and Fluids 197. doi:10.1016/j.compfluid.2019.104371.
[49] S. Diot, La méthode MOOD, la premiére approache a posteriori aux méthodes volumes finis d'ordre trés élevé, PhD Thesis (2012) 1–191. URL http://thesesups.ups-tlse.fr/1736/
[50] J. Fernandez-Fidalgo, L. Ramirez, P. Tsoutsanis, I. Colominas, X. Nogueira, A reduced-dissipation weno scheme with automatic dissipation adjustment, Journal of Computational Physics 425. doi:10.1016/j.jcp.2020.109749.
[51] J. Zhu, X. Zhong, C.-W. Shu, J. Qiu, Runge-Kutta discontinuous Galerkin method with a simple and compact Hermite WENO limiter on unstructured meshes, Communications in Computational Physics 21 (3) (2017) 623–649.
[52] V. Titarev, P. Tsoutsanis, D. Drikakis, WENO schemes for mixed-element unstructured meshes, Communications in Computational Physics 8 (3) (2010) 585–609.
[53] W. Boscheri, M. Semplice, M. Dumbser, Central WENO subcell finite volume limiters for ADER discontinuous Galerkin schemes on fixed and moving unstructured meshes, Communications in Computational Physics 25 (2) (2019) 311–346. doi:10.4208/cicp.OA-2018-0069.
[54] Z. Zhao, Y. Chen, J. Qiu, A hybrid Hermite WENO scheme for hyperbolic conservation laws, Journal of Computational Physics 405. doi:10.1016/j.jcp.2019.109175.
[55] D. Balsara, S. Garain, V. Florinski, W. Boscheri, An efficient class of WENO schemes with adaptive order for unstructured meshes, Journal of Computational Physics 404. doi:10.1016/j.jcp.2019.109062.
[56] E. F. Toro, V. A. Titarev, Derivative Riemann solvers for systems of conservation laws and ADER methods, Journal of Computational Physics 212 (1) (2006) 150–165.
[57] V. A. Titarev, E. F. Toro, ADER schemes for three-dimensional nonlinear hyperbolic systems, Journal of Computational Physics 204 (2005) 715–736.
[58] S. Busto, E. Toro, E. Vázquez-Cendón, Design and analysis of ADER-type schemes for model advection–diffusion–reaction equations, Journal of Computational Physics 327 (2016) 553–575.
[59] S. Busto, S. Chiocchetti, M. Dumbser, E. Gaburro, I. Peshkov, High order ADER schemes for continuum mechanics, Frontiers in Physics 8 (2020) 32. doi:10.3389/fphy.2020.00032.
[60] J. Friedrich, O. Kolb, Maximum principle satisfying CWENO schemes for nonlocal conservation laws, SIAM Journal on Scientific Computing 41 (2) (2019) A973–A988. doi:10.1137/18M1175586.
[61] M. Semplice, G. Visconti, Efficient implementation of adaptive order reconstructions, Journal of Scientific Computing 83 (1). doi:10.1007/s10915-020-01156-6.
[62] I. Cravero, G. Puppo, M. Semplice, G. Visconti, Cool WENO schemes, Computers and Fluids 169 (2018) 71–86. doi:10.1016/j.compfluid.2017.07.022.
[63] K. Cooley, J. Baeder, A central compact-reconstruction WENO method for hyperbolic conservation laws, no. 210059, 2018, pp. 36–45.
[64] E. Gaburro, W. Boscheri, S. Chiocchetti, C. Klingenberg, V. Springel, M. Dumbser, High order direct Arbitrary-Lagrangian-Eulerian schemes on moving Voronoi meshes with topology changes, Journal of Computational Physics 407 (2020) 109167.
[65] M. Semplice, A. Coco, G. Russo, Adaptive mesh refinement for hyperbolic systems based on third-order compact WENO reconstruction, Journal of Scientific Computing 66 (2) (2016) 692–724.
[66] D. Levy, G. Puppo, G. Russo, Compact central WENO schemes for multidimensional conservation laws, SIAM Journal of Scientific Computing 22 (2000) 656–672.
[67] J. Zhu, J. Qiu, New finite volume weighted essentially nonoscillatory schemes on triangular meshes, SIAM Journal of Scientific Computing 40 (2018) A903–A928.
[68] J. Zhu, C.-W. Shu, A new type of third-order finite volume multi-resolution WENO schemes on tetrahedral meshes, Journal of Computational Physics 406 (2020) 109212.
[69] J. Zhu, C.-W. Shu, J. Qiu, High-order Runge-Kutta discontinuous Galerkin methods with a new type of multi-resolution WENO limiters on triangular meshes, Applied Numerical Mathematics 153 (2020) 519–539. doi:10.1016/j.apnum.2020.03.013.
[70] H. Zhu, J. Qiu, J. Zhu, A simple, high-order and compact WENO limiter for RKDG method, Computers and Mathematics with Applications 79 (2) (2020) 317–336. doi:10.1016/j.camwa.2019.06.034.
[71] J. Zhu, J. Qiu, C.-W. Shu, High-order Runge-Kutta discontinuous Galerkin methods with a new type of multi-resolution WENO limiters, Journal of Computational Physics 404. doi:10.1016/j.jcp.2019.109105.
[72] P. Tsoutsanis, Stencil selection algorithms for WENO schemes on unstructured meshes, Journal of Computational Physics: X 4. doi:10.1016/j.jcpx.2019.100037.
[73] UCNS3D cfd code, http://www.ucns3d.com, accessed: 04-03-2021.
[74] A. Stroud, Approximate Calculation of Multiple Integrals, Prentice-Hall Inc., Englewood Cliffs, New Jersey, 1971.
[75] F. Ricci, P. Silva, P. Tsoutsanis, A. Antoniadis, Hovering rotor solutions by high-order methods on unstructured grids, Aerospace Science and Technology 97. doi:10.1016/j.ast.2019.105648.
[76] A. Antoniadis, P. Tsoutsanis, D. Drikakis, Numerical accuracy in rans computations of high-lift multi-element airfoil and aircraft configurations, in: 53rd AIAA Aerospace Sciences Meeting, Vol. 0317, 2015. doi:10.2514/6.2015-0317.
[77] P. Silva, P. Tsoutsanis, A. Antoniadis, Simple multiple reference frame for high-order solution of hovering rotors with and without ground effect, Aerospace Science and Technology 111. doi:10.1016/j.ast.2021.106518.
[78] A. Antoniadis, P. Tsoutsanis, D. Drikakis, High-order schemes on mixed-element unstructured grids for aerodynamic flows, in: 42nd AIAA Fluid Dynamics Conference and Exhibit, Vol. 2833, 2012. doi:10.2514/6.2012-2833.

[79] A. Antoniadis, P. Tsoutsanis, I. Kokkinakis, Z. Rana, D. Drikakis, Azure: An advanced CFD software suite based on high-resolution and high-order methods, in: 53rd AIAA Aerospace Sciences Meeting, Vol. 0813, 2015. doi:10.2514/6.2015-0813.
[80] A. Antoniadis, D. Drikakis, I. W. Kokkinakis, P. Tsoutsanis, Z. Rana, High-order methods for hypersonic shock wave turbulent boundary layer interaction flow, in: 20th AIAA International Space Planes and Hypersonic Systems and Technologies Conference, Vol. 3524, 2015. doi:10.2514/6.2015-3524.
[81] P. Tsoutsanis, I. Kokkinakis, L. Konozsy, D. Drikakis, R. Williams, D. Youngs, Comparison of structured- and unstructured-grid, compressible and incompressible methods using the vortex pairing problem, Computer Methods in Applied Mechanics and Engineering 293 (2015) 207–231. doi:10.1016/j.cma.2015.04.010.
[82] P. Tsoutsanis, H. Srinivasan, Adaptive mesh refinement techniques for high-order finite-volume WENO schemes, in: ECCOMAS Congress 2016, Crete, Greece, 2016. doi:https://doi.org/10.7712/100016.2003.8544.
[83] P. Tsoutsanis, N. Simmonds, A. Gaylard, Implementation of a low-Mach number modification for high-order finite-volume schemes for arbitrary hybrid unstructured meshes, in: ECCOMAS Congress 2016, Crete, Greece, 2016. doi:https://doi.org/10.7712/100016.2004.8545.
[84] P. Tsoutsanis, D. Drikakis, Addressing the challenges of implementation of high-order finite-volume schemes for atmospheric dynamics on unstructured meshes, in: ECCOMAS Congress 2016, Crete, Greece, 2016. doi:https://doi.org/10.7712/100016.1846.8406.
[85] N. Simmonds, P. Tsoutsanis, A. Antoniadis, K. Jenkins, A. Gaylard, Low-mach number treatment for finite-volume schemes on unstructured meshes, Applied Mathematics and Computation 336 (2018) 368–393.
[86] P. Tsoutsanis, A. Antoniadis, K. Jenkins, Improvement of the computational performance of a parallel unstructured WENO finite volume cfd code for implicit large eddy simulation, Computers and Fluids 173 (2018) 157–170. doi:10.1016/j.compfluid.2018.03.012.
[87] M. Dumbser, M. Castro, C. Pares, E. Toro, ADER schemes on unstructured meshes for nonconservative hyperbolic systems: Applications to geophysical flows, Computers and Fluids 38 (9) (2009) 1731–1748.
[88] A. Jalali, C. Ollivier-Gooch, Higher-order finite volume solution reconstruction on highly anisotropic meshes, 21st AIAA Computational Fluid Dynamics Conference, 2013.
[89] X. Nogueira, L. Cueto-Felgueroso, I. Colominas, F. Navarrina, M. Casteleiro, A new shock-capturing technique based on moving least squares for higher-order numerical schemes on unstructured grids, Computer Methods in Applied Mechanics and Engineering 199 (37-40) (2010) 2544–2558.
[90] G. W. Stewart, Matrix Algorithms, Volume 1: Basic Decompositions, Society for Industrial and Applied Mathematics SIAM, 1998.
[91] V. Titarev, E. Toro, Finite-volume WENO schemes for three-dimensional conservation laws, Journal of Computational Physics 201 (1) (2004) 238–260.
[92] A. Harten, B. Engquist, S. Osher, S. Chakravarthy, Uniformly high order accurate essentially non-oscillatory schemes, iii, Journal of Computational Physics 71 (2) (1987) 231–303.
[93] R. Borges, M. Carmona, B. Costa, W. Don, An improved weighted essentially non-oscillatory scheme for hyperbolic conservation laws, Journal of Computational Physics 227 (2008) 3191–3211.
[94] M. Castro, B. Costa, W. Don, High order weighted essentially non-oscillatory WENO-Z schemes for hyperbolic conservation laws, Journal of Computational Physics 230 (2011) 1766–1792.
[95] I. Cravero, M. Semplice, G. Visconti, Optimal definition of the nonlinear weights in multidimensional central wenoz reconstructions, SIAM Journal on Numerical Analysis 57 (5) (2019) 2328–2358. doi:10.1137/18M1228232.
[96] E. Toro, M. Spruce, W. Speares, Restoration of the contact surface in the HLL-Riemann solver, Shock Waves 4 (1) (1994) 25–34.
[97] H. Nishikawa, Robust and accurate viscous discretisation via upwind scheme-i: Basic principle, Computer and Fluids 49 (2011) 62–86.
[98] A. Jalali, M. Sharbatdar, C. Ollivier-Gooch, Accuracy analysis of unstructured finite volume discretization schemes for diffusive fluxes, Computer and Fluids 101 (2014) 220–232.
[99] G. Gassner, F. Lorcher, C. Munz, A contribution to the construction of diffusion fluxes for finite volume and discontinuous Galerkin schemes, Journal of Computational Physics 224 (2) (2007) 1049–1063.
[100] R. J. Spiteri, S. J. Ruuth, A new class of optimal high-order strong-stability-preserving time-stepping schemes, SIAM Journal of Numerical Analysis 40 (2) (2002) 469–491.
[101] P. Tsoutsanis, Knl performance comparison: Ucns3d, ARCHER performance report.
URL www.archer.ac.uk/community/benchmarks/archer-knl/KNL_perf_UCNS3D.pdf
[102] D. Balsara, C.-W. Shu, Monotonicity preserving weighted essentially non-oscillatory schemes with increasingly high order of accuracy, Journal of Computational Physics 160 (2) (2000) 405–452.
[103] R. Leveque, High-resolution conservative algorithms for advection in incompressible flow, SIAM Journal on Numerical Analysis 33 (2) (1996) 627–665. doi:10.1137/0733033.
[104] C.-W. Shu, S. Osher, Efficient implementation of essentially non-oscillatory shock-capturing schemes, ii, Journal of Computational Physics 83 (1) (1989) 32–78.
[105] C. W. Schulz-Rinner, J. Collines, H. M. Glaz, Numerical solution of the Riemann problem for two-dimensional gas dynamics, SIAM Journal of Scientific Computing 7 (1993) 1394–1414.
[106] D. Drikakis, C. Fureby, F. Grinstein, D. Youngs, Simulation of transition and turbulence decay in the Taylor-Green vortex, Journal of Turbulence 8 (2007) 1–12.
[107] M. Dumbser, I. Peshkov, E. Romenski, O. Zanotti, High order ADER schemes for a unified first order hyperbolic formulation of continuum mechanics: Viscous heat-conducting fluids and elastic solids, Journal of Computational Physics 314 (2016) 824–862.
[108] J.-B. Chapelier, M. de la Llave Plata, E. Lamballais, Development of a multiscale LES model in the context of a modal discontinuous Galerkin method, Computer Methods in Applied Mechanics and Engineering 307 (2016) 275–299.
[109] A. Sifounakis, S. Lee, D. You, A conservative finite volume method for incompressible Navier-Stokes equations on locally refined nested cartesian grids, Journal of Computational Physics 326 (2016) 845–861.
[110] C.-W. Shu, W.-S. Don, D. Gottlieb, O. Schilling, L. Jameson, Numerical convergence study of nearly incompressible, inviscid Taylor-Green vortex flow, Journal of Scientific Computing 24 (1) (2005) 569–595.

[111] M. Brachet, D. Meiron, B. Nickel, R. Morf, U. Frisch, S. Orszag, Small-scale structure of the Taylor-Green vortex, Journal of Fluid Mechanics 130 (1983) 411–452. doi:10.1017/S0022112083001159.
[112] F. Fambri, M. Dumbser, Spectral semi-implicit and space-time discontinuous Galerkin methods for the incompressible Navier-Stokes equations on staggered Cartesian grids, Applied Numerical Mathematics 110 (2016) 41–74.
[113] F. Fambri, M. Dumbser, Semi-implicit discontinuous Galerkin methods for the incompressible Navier-Stokes equations on adaptive staggered Cartesian grids, Computer Methods in Applied Mechanics and Engineering 324 (2017) 170–203.
[114] M. Tavelli, M. Dumbser, A staggered space-time discontinuous Galerkin method for the three-dimensional incompressible Navier-Stokes equations on unstructured tetrahedral meshes, Journal of Computational Physics 319 (2016) 294 – 323.
[115] M. Tavelli, M. Dumbser, A pressure-based semi-implicit space-time discontinuous Galerkin method on staggered unstructured meshes for the solution of the compressible Navier-Stokes equations at all Mach numbers, Journal of Computational Physics 341 (2017) 341–376.
[116] H. Schardin, High frequency cinematography in the shock tube, Journal of Photographic Science 2 (1957) 17–19.
[117] S.-M. Chang, K.-S. Chang, On the shock vortex-interaction in Schardin's problem, Shock Waves 10 (2000) 333–343.
[118] A. Kravchenko, P. Moin, Numerical studies of flow over a circular cylinder at Re=3900, Physics of Fluids 12 (2) (2000) 403–417. doi:10.1063/1.870318.
[119] L. Ong, J. Wallace, The velocity field of the turbulent very near wake of a circular cylinder, Experiments in Fluids 20 (6) (1996) 441–453. doi:10.1007/BF00189383.
[120] M. Breuer, Large eddy simulation of the subcritical flow past a circular cylinder: Numerical and modeling aspects, International Journal for Numerical Methods in Fluids 28 (9) (1998) 1281–1302.
[121] X. Ma, G.-S. Karamanos, G. Karniadakis, Dynamics and low-dimensionality of a turbulent near wake, Journal of Fluid Mechanics 410 (2000) 29–65. doi:10.1017/S0022112099007934.
[122] J. Kim, H. Choi, Distributed forcing of flow over a circular cylinder, Physics of Fluids 17 (3) (2005) 033103–1–033103–16. doi:10.1063/1.1850151.
[123] J. Franke, W. Frank, Large eddy simulation of the flow past a circular cylinder at Re= 3900, Journal of Wind Engineering and Industrial Aerodynamics 90 (10) (2002) 1191–1206. doi:10.1016/S0167-6105(02)00232-5.
[124] A. Beck, T. Bolemann, D. Flad, H. Frank, G. Gassner, F. Hindenlang, C.-D. Munz, High-order discontinuous Galerkin spectral element methods for transitional and turbulent flow simulations, International Journal for Numerical Methods in Fluids 76 (8) (2014) 522–548. doi:10.1002/fld.3943.
[125] D. Lysenko, I. Ertesvag, K. Rian, Large-eddy simulation of the flow over a circular cylinder at Reynolds number 3900 using the openfoam toolbox, Flow, Turbulence and Combustion 89 (4) (2012) 491–518. doi:10.1007/s10494-012-9405-0.
[126] Z. Xia, X. Zuoli, S. Yipeng, C. Shiyi, Mach number effect of compressible flow around a circular cylinder, AIAA Journal 54 (6) (2016) 2004–2009. doi:10.2514/1.J054420.
[127] C. Welsh, The drag of finite length cylinders determined from flight tests at high reynolds numbers for a mach number range from 0.5 to 1.3, NACA TN (2941).
[128] J. Macha, Drag of circular cylinders at transonic mach numbers, Journal of Aircraft 14 (6) (1977) 605–607. doi:10.2514/3.58828.
[129] D. Canuto, K. Taira, Two-dimensional compressible viscous flow around a circular cylinder, Journal of Fluid Mechanics 785 (2015) 349–371. doi:10.1017/jfm.2015.635.
[130] L. Fu, A very-high-order TENO scheme for all-speed gas dynamics and turbulence, Computer Physics Communications 244 (2019) 117–131. doi:10.1016/j.cpc.2019.06.013.
[131] L. Fu, X. Hu, N. Adams, Targeted ENO schemes with tailored resolution property for hyperbolic conservation laws, Journal of Computational Physics 349 (2017) 97–121. doi:10.1016/j.jcp.2017.07.054.
[132] L. Fu, X. Hu, N. Adams, A family of high-order targeted ENO schemes for compressible-fluid simulations, Journal of Computational Physics 305 (2016) 333–359. doi:10.1016/j.jcp.2015.10.037.
[133] I. Peshkov, E. Romenski, A hyperbolic model for viscous Newtonian flows, Continuum Mechanics and Thermodynamics 28 (2016) 85–104.
[134] M. Dumbser, I. Peshkov, E. Romenski, O. Zanotti, High order ADER schemes for a unified first order hyperbolic formulation of continuum mechanics: Viscous heat-conducting fluids and elastic solids, Journal of Computational Physics 314 (2016) 824–862.
[135] C. Bassi, L. Bonaventura, S. Busto, M. Dumbser, A hyperbolic reformulation of the Serre-Green-Naghdi model for general bottom topographies, Computers & Fluids 212 (2020) 104716.
[136] S. Busto, M. Dumbser, C. Escalante, N. Favrie, S. Gavrilyuk, On high order ADER discontinuous Galerkin schemes for first order hyperbolic reformulations of nonlinear dispersive systems, Journal of Scientific ComputingSubmitted.
[137] S. Busto, M. Tavelli, W. Boscheri, M. Dumbser, Efficient high order accurate staggered semi-implicit discontinuous Galerkin methods for natural convection problems, Computers and Fluids 198 (2020) 104399.
[138] A. Bermúdez, S. Busto, M. Dumbser, J. Ferrín, L. Saavedra, M. Vázquez-Cendón, A staggered semi-implicit hybrid FV/FE projection method for weakly compressible flows, Journal of Computational Physics 421 (2020) 109743.

Credit author statement.

Dr P Tsoutsanis
Cranfield University
Cranfield University, Cranfield MK43 0AL, United Kingdom
Prof. M. Dumbser
University of Trento, via Mesiano 77, Trento, 38123, Italy

Title: “Arbitrary High Order Central Non-Oscillatory Schemes on Mixed-Element Unstructured Meshes” for consideration by the Computer and Fluids.

Credit author statement

Panagiotis Tsoutsanis: Conceptualisation, Methodology, Data curation, Writing-Original Draft preparation, visualization, Software, Investigation, Validation; Writing-Reviewing and Editing

Michael Dumbser: Conceptualisation, Methodology, Writing-Reviewing and Editing

Dr P Tsoutsanis, Prof. M. Dumbser

Declaration of Interest Statement

Arbitrary High Order Central Non-Oscillatory Schemes on Mixed-Element Unstructured Meshes

Declaration of interest: none

Dr P. Tsoutsanis
Cranfield University
Cranfield University, Cranfield MK43 0AL, United Kingdom

Prof. M. Dumbser
University of Trento, via Mesiano 77, Trento, 38123, Italy

https://dspace.org/

Arbitrary high order central non-oscillatory schemes on mixed-element unstructured meshes

Tsoutsanis, Panagiotis; Dumbser, Michael

2021-04-29
Elsevier
https://doi.org/10.1016/j.compfluid.2021.104961
Tsoutsanis P, Dumbser M. (2021) Arbitrary high order central non-oscillatory schemes on mixed-element unstructured meshes. Computers and Fluids, Volume 225, July 2021, Article number 104961

Downloaded from a DSpace repository. https://dspace.org/